atmosphere

MDPI

Article

A Modeling Study of the Impacts of 3-Dimensional Topography on Shallow-Convective Clouds

Yunzuo He [1,2], Mingxin Gong [1,2], Shizuo Fu [1,2,*] and Xin Deng [3]

[1] Institute of Geography, Fujian Normal University, Fuzhou 350007, China
[2] Key Laboratory for Humid Subtropical Eco-Geographical Processes of the Ministry of Education, Fujian Normal University, Fuzhou 350007, China
[3] College of Agriculture, Fujian Agriculture and Forestry University, Fuzhou 350007, China
* Correspondence: fusz@fjnu.edu.cn; Tel.: +86-18810506411

Abstract

Shallow-convective clouds (SCCs) play important roles in the Earth's atmospheric system by affecting radiative balance, large-scale circulation, and transport of pollutants. It is common sense that topography exerts substantial impacts on SCCs. However, the underlying mechanisms are not well understood. Here, we performed large-eddy simulations (LESs) to investigate how three-dimensional (3D) topography affected SCCs. The 3D topography was constructed using two widely used two-dimensional (2D) topographies, a bell-shaped ridge varying in the x-direction and a series of sinusoidal ridges varying in the y-direction. The bell-shaped ridge was the major ridge. The upper parts and lower parts of the sinusoidal ridges were the minor ridges and minor valleys, respectively. The wavelength of the sinusoidal ridges was systematically varied. LESs were also performed separately using the 2D topographies. In the simulations with 3D topography, the upslope winds were mainly over the minor ridges and the return flows were mainly over the minor valleys, which was different from those in the simulations using 2D topographies. The upslope winds promoted the development of SCCs over the major ridges by producing large thermals and high humidity, similar to in the simulations using 2D topographies. Increasing the wavelength of minor ridges enlarged the region with convergence, and thereby increased the size of SCCs. Our results suggest that it is necessary to consider the 3D topography instead of the more conventional 2D topographies when investigating the topographic impacts on SCCs.

Keywords: shallow-convective clouds; large eddy simulation; 3-Dimensional topography

Check for updates

Academic Editor: Hao Luo

Received: 17 January 2026
Revised: 23 February 2026
Accepted: 25 February 2026
Published: 27 February 2026

Copyright: © 2026 by the authors. Licensee MDPI, Basel, Switzerland. This article is an open access article distributed under the terms and conditions of the Creative Commons Attribution (CC BY) license.

1. Introduction

Shallow-convective clouds (SCCs) frequently appear around the world [1–3]. They efficiently reflect solar radiation and thereby cool the Earth's surface [4]. They exchange momentum in the presence of vertical wind shear and thereby affect large-scale circulation [5,6]. They transport pollutants out of the boundary layer [7] and thereby facilitate the long-range transport of pollutants [8]. They can also transport moisture from within the boundary layer to above the boundary layer, creating a favorable environment for deep-convective clouds [9–12].

The sizes of SCCs are typically around 1 km or smaller in size [13,14], so they cannot be resolved by current climate models [15] or weather forecasting models [16]. Nevertheless, SCCs actively interact with larger-scale weather systems [17]. Their impacts can only

be included through parameterization [18]. Since most previous parameterizations were established for SCCs over homogeneous surfaces [19–21], they did not take the topographic impacts into consideration. Obviously, a deep understanding of the topographic impacts on SCCs is necessary before one can implement the impacts into parameterizations.

Cloud size is one of the most important parameters describing SCCs [14,22]. If a cloud is large, its core is better-protected and can continue to develop, and if a cloud is small, it dissipates quickly [23]. By tracking the life cycles of SCCs simulated by large-eddy simulations (LESs), it was found that clouds that are bigger at their bases are also bigger at upper levels and develop to higher levels [24]. Similar results are also obtained for deep-convective clouds [25].

SCCs are closely tied to thermals in the convective boundary layer [26,27]. Over flat homogeneous ground, observational and modeling studies showed that the thermals below larger SCCs are larger and stronger [28,29]. When the flat ground is heterogeneous in soil moisture, local circulations develop and increase the size of the below-cloud thermals, and thereby increase the size of SCCs [30]. Note that the effect of surface heterogeneity is prominent only when the ambient wind is sufficiently weak [31].

Mountainous/hilly terrain covers more than 50% of the global land surface [32]. The presence of topography exerts substantial impacts on SCCs. By analyzing high-resolution satellite data, it was found that both the number and size of SCCs increased with elevation [14]. In particular, the topographic impacts on cloud size were prominent for large SCCs (those larger than the 90th percentiles) and negligible for smaller SCCs. A later LES study systematically investigated the impacts of isolated two-dimensional (2D) ridges on SCCs by varying the maximum height and half-width of the ridge [33]. It was found that both the temperature and the number of ascending grid points over the ridge top increased with the maximum height and/or the half-width. Humidity over the ridge top increased with the maximum height when the half-width was small, and had no systematic variation when the half-width was large. The humidity also decreased with the half-width. As a result of the synergistic effects of temperature, humidity, and updrafts, the depth of SCCs increased with the maximum height. It also increased with the half-width when the half-width was less than 8 km, and remained nearly constant when the half-width was further increased.

Although previous studies that used 2D ridges have provided useful insights into the topographic impacts on SCCs, they could not capture the full complexity of the topographic impacts on SCCs. Our everyday experience clearly suggests that real topography is never as simple as a 2D ridge. In order to advance our understanding of topographic impacts on SCCs, this study investigated how three-dimensional (3D) topography affected SCCs. The 3D topography was constructed by idealizing the topography of real ridges. It consists of two types of idealized and widely used 2D topography, an isolated bell-shaped ridge [34] and a series of sinusoidal ridges [35]. The axes of the sinusoidal ridges are perpendicular to the axis of the bell-shaped ridge. To facilitate the interpretation of the results of 3D topography, we also separately investigated how the 2D bell-shaped ridge and sinusoidal ridges affected SCCs. Section 2 presents the methods. Section 3 presents in sequence the results of the 2D bell-shaped ridge, 2D sinusoidal ridges, and 3D topography. A summary is provided in Section 4.

2. Materials and Methods

2.1. Model

We used release 19.10 of Cloud Model 1(CM1) [36] to perform the simulations. The compressible governing equations are solved using the time-splitting method [37]. The fifth-order advection scheme is used for momentum [38]. The fifth-order weighted, essentially

non-oscillatory scheme is used for scalars [39]. The terrain-following coordinate is used to treat the topography [40]. CM1 was configured as an LES, where the sub-filter-scale turbulence is treated with the turbulent kinetic energy scheme [41]. Cloud microphysics is parameterized with a two-moment microphysics scheme [42]. Radiative transfer is not considered and surface heat fluxes are prescribed. An earlier study of topographic impacts on SCCs found that the results were qualitatively the same when radiative transfer and interactive surface heat fluxes were used [33]. The setup of this study is similar to that of existing research [33], except that 3D topography instead of 2D topography is used.

2.2. Case

Figure 1 shows a satellite image of SCCs developing above the parallel ridges in eastern Sichuan, China. The underlying topography is the Advanced Spaceborne Thermal Emission and Reflection Radiometer (ASTER) Global Digital Elevation Model version 2 (GDEMV2). The cloud image is from Landsat-8 on 2 August 2021. Both the GDEMV2 and Landsat-8 images have resolutions of 30 m. The white pixels in Figure 2b,c indicate clouds, which were identified using the haze-optimized transformation [43]. Figure 1b clearly shows that SCCs developed over the ridges and did not develop over the surrounding areas. Figure 1c further reveals that the ridge is not homogeneous along the major axis, which is along the southwest–northeast direction. Instead, there are many minor ridges and minor valleys attached to the major ridge. More importantly, it is obvious that the presence of the minor ridges and minor valleys affected the positions of the SCCs.

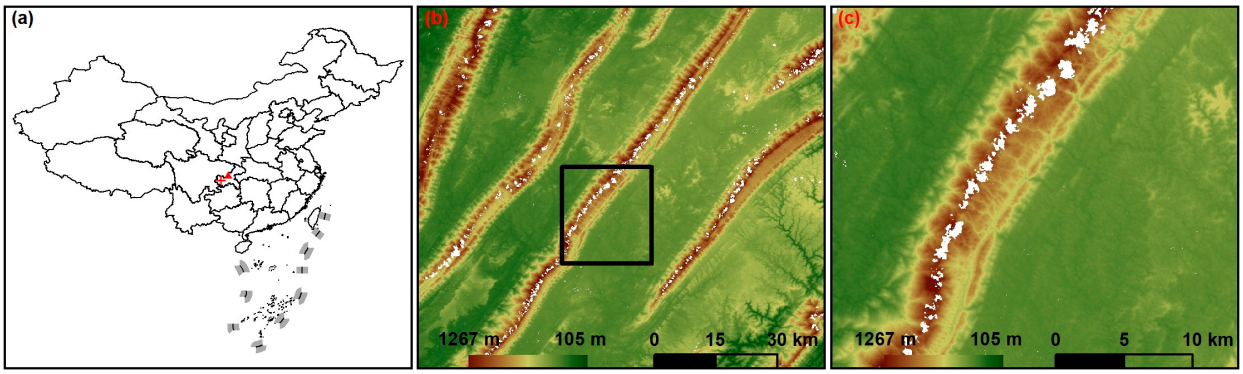

Figure 1. (**a**) The red triangle indicates the position of the parallel ridges and valleys in eastern Sichuan. The red cross indicates Chongqing station. (**b**) SCCs, which are in white, and the parallel ridges. (**c**) The same as (**b**) except for the region enclosed by the black box in (**b**). The cloud information is from Landsat-8 on 2 August 2021. Landsat-8 crosses the equator at 10:00 ± 15 min local time.

A sounding from Chongqing station (red cross in Figure 1a), obtained at 08:00 on the same day, is shown in Figure 2. The atmosphere is stable below z = 2 km, as revealed by the fact that the potential temperature increases with height (Figure 2b). The humidity is high below z = 0.8 km, and quickly decreases with height at higher levels (Figure 2c). A remarkable inversion is seen around 600 hPa, which corresponds to z = 4400 m. According to the ERA5 reanalysis data [44], the surface sensible heat flux and latent heat flux both exhibit near-perfect sinusoidal variations, as expected from the low cloud fraction (Figure 1b). In our simulations, the total heat flux (THF) follows a sinusoidal variation $THF = THF_m \sin(2\pi t/24)$, where THF_m is the maximum THF and is 600 W m^{-2}; and t is time in h. The Bowen ratio is 0.16. Note that the simulation starts at t = 0 h and lasts for 6 h. The ambient wind is set to zero for simplicity. It is worth mentioning that even an ambient wind as weak as 3 m s^{-1} can substantially modify the results [45]. In addition, Coriolis force was not considered because the topography is small [34].

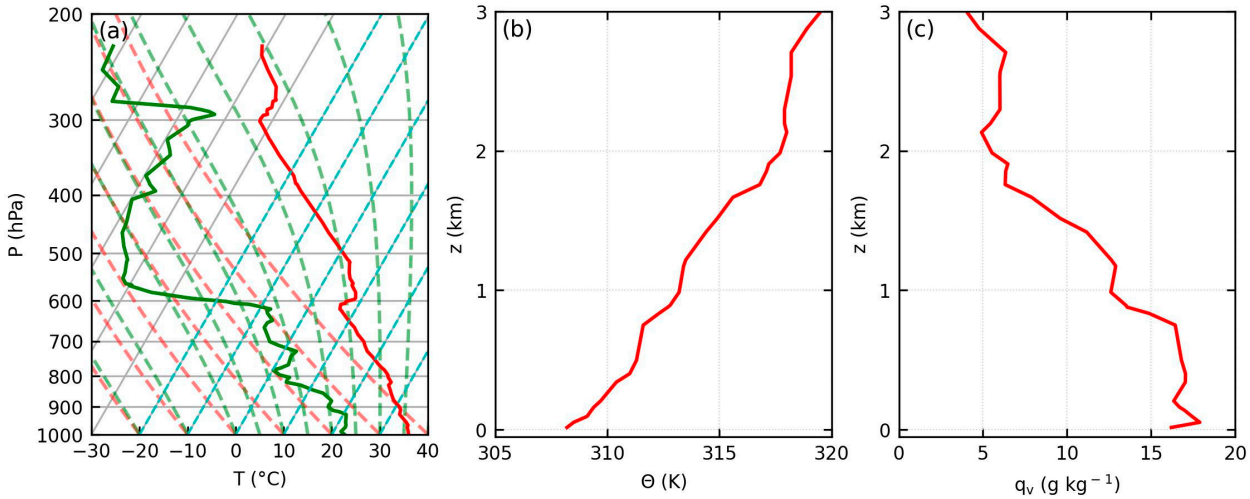

Figure 2. (**a**) The sounding used to initialize the simulations. The corresponding profiles of potential temperature and vapor mixing ratio below z = 3 km are shown in (**b**) and (**c**), respectively. The sounding was from Chongqing station at 08:00 on 2 August 2021.

2.3. Experimental Setup

As shown in Figure 1c, the real 3D topography consists of a major ridge and multiple minor ridges and minor valleys. Hereafter, the direction perpendicular to the major ridge is the x-direction, the direction along the major ridge is the y-direction, and the vertical direction is the z-direction. The 3D topography used in the simulations is a simplified version of the real 3D topography

$$z_{t,3D} = H_m\, f_{x2} + H_m\, (f_{x1} - f_{x2})\, f_y \tag{1}$$

where H_m is the maximum height. The variations in the x-direction are described by two bell-shaped functions

$$f_{x1} = \frac{1}{1 + (x\ /\ W_{x1})^2} \tag{2}$$

$$f_{x2} = \frac{1}{1 + (x\ /\ W_{x2})^2} \tag{3}$$

where W_{x1} and W_{x2} are the half-widths in the x-direction. When $W_{x1} > W_{x2}$, f_{x1} describes the topographic variations in the minor ridges and f_{x2} describes the topographic variations in the minor valleys. The variation in the y-direction is sinusoidal.

$$f_y = 0.5\,[1 + \sin(2\pi y\ /\ W_y)] \tag{4}$$

where W_y is the wavelength in the y-direction. The 3D topography is obtained by adding the parts described by the term $H_m\, (f_{x1} - f_{x2})\, f_y$ to the 2D ridge described by $H_m\, f_{x2}$. An example of a 3D topography is shown in Figure 3a.

We set H_m = 700 m, W_{x1} = 2000 m, and W_{x2} = 1000 m. A series of simulations were performed with different values of W_y, i.e., 1400, 1800, 2200, 3000, 4600, and 7800 m. These values were selected according to the real topography shown in Figure 1b. These simulations are called the 3D simulations. We use Simulation 3D_1400 to refer to the 3D simulation with W_y of 1400 m. Similar nomenclature is used for the other 3D simulations. We do not investigate the impacts of varying H_m, W_{x1}, or W_{x2} for two reasons. On the one hand, performing LESs is rather expensive, so we cannot afford exploring an even wider parameter space. On the other hand, our results suggest that the impacts of varying H_m,

W_{x1}, or W_{x2} of 3D topography can be understood by investigating the impacts of varying H_m or W_x of 2D topography; and the latter has been done by a previous study [33].

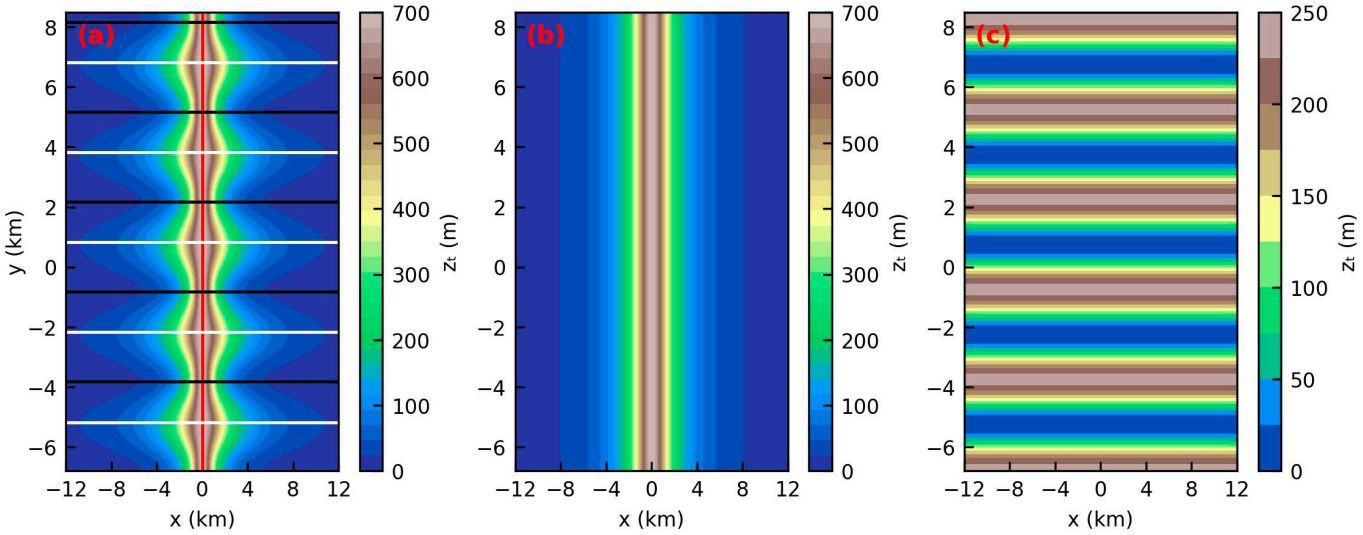

Figure 3. (**a**) A 3D topography with H_m = 700 m, W_{x1} = 2000 m, W_{x2} = 1000 m, and W_y = 3000 m. The red line, white lines, and black lines indicate the major ridge, minor ridges, and minor valleys, respectively. (**b**) An isolated bell-shaped ridge with H_m = 700 m and W_x = 1500 m. (**c**) A series of parallel ridges with H_m = 700 m and W_y = 3000 m.

In order to lay a foundation for understanding the impacts of 3D topography on SCCs, we performed another two sets of simulations to investigate the impacts of 2D topography on SCCs. Such a strategy was also adopted in previous studies [46]. In the first set, the topography is described by

$$z_{t,2DX} = H_m \, f_x \tag{5}$$

Here $f_x = \frac{1}{1 + (x \,/\, W_x)^2}$. Three values are tested for W_x, i.e., 1000, 1500, and 2000 m. Note that the first value equals W_{x1} and the third value equals W_{x2} of the 3D simulations. An example of a 2D topography described by Equation (5) is shown in Figure 3b. These simulations are called 2DX simulations. Simulation 2DX_1000 refers to the 2DX simulation with W_x of 1000 m. The other 2DX simulations are named similarly. In the second set, the topography is described by

$$z_{t,2DY} = H_m \, D \, f_y \tag{6}$$

Here $D = \max(f_{x1} - f_{x2})$. The term $H_m \, D$ describes the amplitude of the variation and equaled 233 m. W_y takes the same values for the 3D simulations. An example of a 2D topography described by Equation (6) is shown in Figure 3c. These simulations are called the 2DY simulations. Simulation 2DY_1400 refers to the 2DY simulation with W_y of 1400 m. The other 2DY simulations are named similarly. We note that the slope of the topography in the y-direction is larger in the 2DY simulations than its counterpart in the 3D simulations because $(f_{x1} - f_{x2}) \leq max(f_{x1} + f_{x2})$.

The domain configurations are listed in Table 1. In the 3D simulations, the domain length in the x-direction L_x = 84 km, and the domain length in the z-direction L_z = 10 km. The domain length in the y-direction L_y is variable because it should be an integer times W_y and the number of grid points should be an integer times the number of cores used for the y-dimension. We also require that $L_y \geq 10 \, W_y$. In the 2DX simulations, L_x and L_z are the same as those of the 3D simulations, and L_y = 30 km because the topography does not vary in the y-direction. In the 2DY simulations, L_y and L_z are the same as those of the 3D

simulations, and L_x = 24 km because the topography does not vary in the x-direction. The domain sizes have been confirmed as adequate [33].

Table 1. Domain configurations of the simulations. L_x, L_y, and L_z indicate the domain lengths in the x-, y-, and z-directions, respectively. For L_x and L_z, the numbers outside the parentheses are the lengths of the whole dimension and those inside the parentheses are the lengths of the high-resolution region.

Simulations	3D	2DX	2DY
W_x (m)	W_{x1} = 2000, W_{x2} = 1000,	1000, 2000, 3000	n/a
W_y (m)	1400, 1800, 2200, 3000, 4600, 7800	n/a	1400, 1800, 2200, 3000, 4600, 7800
L_x (km)	84 (60)	84 (60)	24 (24)
L_y (km)	46.2, 46.8, 46.2, 45, 46, 78	30	46.2, 46.8, 46.2, 45, 46, 78
L_z (km)	10 (4)	10 (4)	10 (4)

In the 3D and 2DX simulations, the resolution in the x-direction is 50 m from $x = -30$ km to 30 km, and is gradually stretched to 350 m from $x = \pm 30$ km to ± 42 km. The resolution in the y-direction is uniformly 50 m. In the 2DY simulations, the resolution in the x-direction is uniformly 50 m. In the regions with negligible topography, the resolution in the z-direction is 40 m below z = 4 km, and is gradually stretched to 200 m at z = 6.4 km, and then remains unchanged. In the regions with topography, the vertical resolution varies with the local terrain height but is still similar to that over the plains. A periodic boundary condition is used in both the x- and y-directions. A Rayleigh damping layer is used above z = 7 km. The results were saved every 10 min.

The 3D and 2DX simulations were initialized with the sounding shown in Figure 2. Perturbations with a maximum amplitude of 0.25 K were added to the initial field of potential temperature to trigger turbulence. For 2DY simulations, no cloud developed when they were initialized in the same manner, because the ridges were too shallow to produce sufficiently strong topographic impacts. We artificially increased the vapor mixing ratio below z = 4 km by 2.8 g kg^{-1}, so that the vapor mixing ratios over the ridges in the 2DY simulations became similar to those over the major ridges in the 3D simulations by the end of the simulations. Clouds are successfully produced with the revised initial profile. For all simulations, the surface heat fluxes are obtained from the ERA5 reanalysis data, as described earlier.

A threshold liquid water path (LWP) was used to define whether a column is cloudy or clear. Previous studies used threshold values of 10 or 20 g m^{-2} [47,48]. However, when these two values were used, it was found that only a small number of huge clouds were produced, because briefly connected clouds were treated as a single cloud. Therefore, a larger threshold LWP, i.e., 50 g m^{-2}, is used. Such a threshold LWP was also used by Reference [49] to define the classical cumulus clouds. Our tests also show that LWP sharply increases from 10 to 50 g m^{-2} near the cloud edges, so using a large threshold LWP has minor impacts on the calculated cloud size. We note that although the clouds might be briefly connected when a smaller threshold LWP is used, the simulated clouds are of a shallow-convective nature. The cloudy columns are four-way connected to define individual clouds. The size of a cloud is defined as $\sqrt{A_c}$, where A_c is the area of the cloud. Section 1 has pointed out that the topographic impacts are prominent for large SCCs but not discernible for smaller SCCs. As a result, the mean size of the largest 10 clouds is used as the representative cloud size for each time.

2.4. Composite Analysis of Thermals

As mentioned in Section 1, the properties of the below-cloud thermals strongly affect the properties of SCCs, so it is necessary to investigate how the topography affects the below-cloud thermals. Individual thermals are chaotic, so it is difficult to analyze the properties of individual thermals. In this study, the thermals were composited and then analyzed. The compositing procedure generally follows that of [9,50].

Due to the use of terrain-following coordinates, the variables on the same grid layer in the terrain-following coordinates are actually at different heights, so the variables were interpolated to a rectangular coordinate system before they were used in the composite analysis. At the height of the cloud base, which was defined as the lowest height with qc $\geq$ 0.01 g kg^{-1}, any grid points with w > 1.2 m s^{-1} were defined as within thermals. These grid points were four-way-connected to form clusters. Each cluster defined a thermal, and its centroid marked the position of the thermal. At each time, only the largest 10 thermals were used to produce the composite thermal. These thermals, along with their surrounding areas, were horizontally shifted so that their centroids coincided. An ensemble averaging was performed over all the coincident thermals to produce the composite thermal. The composite thermals from t = 5 to 6 h were further averaged to produce the final composite thermal. In 2DX simulations, in order to contrast the thermals over the ridges with those over the plains, thermals over the ridges and over the plains were composited separately. Similarly, thermals over the ridges and valleys were computed separately in 2DY simulations and 3D simulations.

The size of the composite thermal was defined as $\sqrt{A_w}$, where A_w was the area of the region with w > 1.2 m s^{-1}. The strength of the composite thermal ($\bar{w}$) is the mean vertical velocity of the region with w > 1.2 m s^{-1}. Mass flux was widely used in cumulus parameterization schemes [51]. It is therefore interesting to investigate how mass flux is related to cloud size. Mass flux was calculated as $F_m = \rho A_w \bar{w}$, where ρ was the air density. As mentioned in Section 1, larger thermals produce larger clouds. As a result, only the largest 10 thermals of each time were composited. This is also consistent with the calculation of cloud size.

From the discussions above, it is clear that the identification of thermals relies on the threshold w. Unfortunately, no guide is available on the selection of the threshold w. We tested multiple values ranging from 0.5 to 2 m s^{-1}. It was found that the results were qualitatively the same when the threshold w was between 1 and 1.5 m s^{-1}. A threshold w smaller than 1 m s^{-1} was inappropriate because it would identify thermals that were too weak to produce clouds. A threshold w larger than 1.5 m s^{-1} was inappropriate because it would exclude thermals that were sufficiently strong to produce weak clouds. Consequently, a threshold w of 1.2 m s^{-1} was adopted.

3. Results

3.1. 2DX Simulations

Figure 4 shows the impacts of the isolated ridge on virtual potential temperature (temperature hereafter), humidity, wind in the x-direction (u-wind), convective available potential energy (CAPE), and convective inhibition (CIN) at t = 6 h in Simulation 2DX_1500. Note that t = 6 h is at the end of the simulation and at the maximum heat fluxes. We use virtual potential temperature instead of potential temperature because the impacts of humidity on local circulations are found to be important. CAPE and CIN were calculated by lifting a parcel possessing the mean property of the lowest 200 m above the local surface. The temperature is higher near the slope than away from the slope (Figure 4a). The associated temperature gradient produces the upslope winds (Figure 4c), which transport vapor to the ridge top and thereby increase the humidity over the ridge top (Figure 4b). The

higher temperature and higher humidity result in larger CAPE (Figure 4d) and near-zero CIN (Figure 4e) over the ridge top. Such an unstable environment favors the development of SCCs. Over the plains, the environment is less favorable for SCCs because of the smaller CAPE and larger CIN.

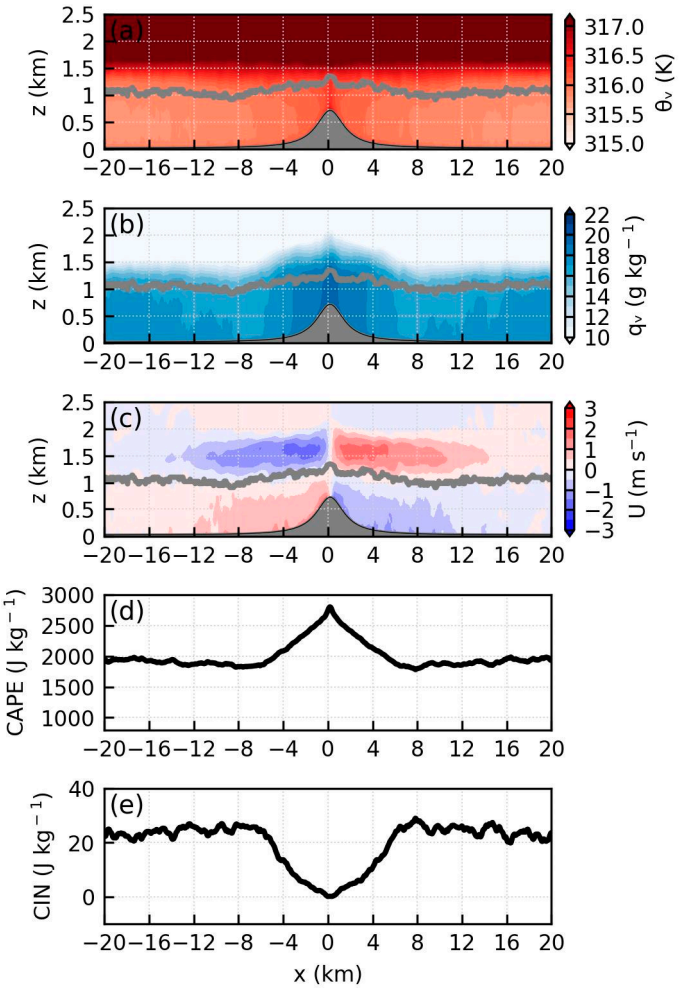

Figure 4. y-averaged (**a**) virtual potential temperature, (**b**) vapor mixing ratio, (**c**) u-wind, (**d**) CAPE, and (**e**) CIN at t = 6 h in Simulation 2DX_1500. The gray lines in (**a**–**c**) indicate the top of the convective boundary layer.

The properties of the composite thermals are shown in Figure 5. Thermals are defined to be over the ridge if they are between $x = -5$ to 5 km, and are defined to be over the plain if they are between x = 20 to 30 km. The composite thermal over the ridge is larger in size than that over the plain (Figure 5a,c). The difference is mainly in the y-direction, due to the convergence of the upslope winds. This is similar to the phenomenon where the thermals were enlarged by the convergence at the sea-breeze front [9,50]. The vertical velocity of the composite thermal over the ridge is slightly larger than that over the plain. The composite thermal also has higher humidity than that over the plain (Figure 5b,d). The temperature difference is negligible. The larger size, stronger vertical velocity, and higher humidity allow the thermals over the ridge to have a stronger potential of developing upward to form SCCs. In all 2DX simulations, SCCs develop over the ridge top and do not develop over the plains, similar to the results of Gong et al. [33].

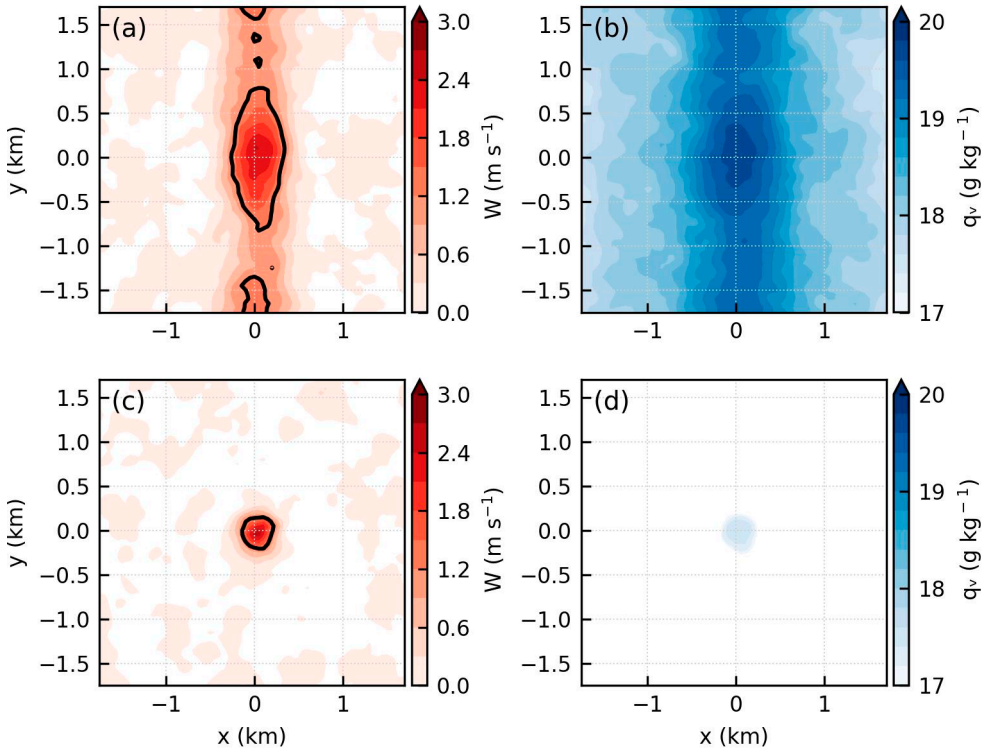

Figure 5. Properties of the composite thermals for Simulation 2DX_1500 from t = 5 to 6 h. (**a**) Vertical velocity, (**b**) vapor mixing ratio of the composite thermal over the ridge. The black line in (**a**) indicates the isoline of 1.2 m s^{-1}. (**c**,**d**) Same as (**a**,**b**) except for the composite thermal over the plain.

The temporal evolutions of virtual potential temperature and vapor mixing ratio are shown in Figure 6a,b. Virtual potential temperature and vapor mixing ratio are quasi-constant in a CBL, so they are represented by the values at the middle of the CBL. Temperature increases with time, both over the ridge top and over the plain, because of the continuous sensible heat flux. At t = 2 h, the temperature over the ridge top is 2 K higher than that over the plain. As seen from Figure 4, the height of the CBL top over the ridge top is almost the same as that over the plain. The presence of topography, therefore, makes the CBL shallower over the ridge top than over the plain, leading to the CBL heating up faster. In the later times, the CBL deepens both over the ridge top and over the plain, so the difference in CBL depth decreases, resulting in a gradually decreasing temperature difference. The humidity over the ridge top is always higher than that over the plain (Figure 6b) because the vapor released from the slopes is transported toward the ridge top, as explained by Reference [33]. Over the ridge top, the humidity first increases with time and then remains quasi-constant. In the early times, the vapor emitted from the surface is more important than the entrainment of dry air at the top of the CBL. In the later times, the CBL becomes so deep that the air at the CBL top is very dry (cf. Figure 2), so the vapor emitted from the surface is mostly counteracted by the impact of entrainment. Over the plains, the humidity increases until t = 3 h and then quickly decreases with time. Since no convergence is available over the plains to provide extra vapor, humidity decreases earlier and faster. The temporal evolution of CAPE is mainly determined by that of humidity (Figure 6c). CIN decreases with time (Figure 6d), both over the ridge top and over the plain, and reaches zero around t = 4.5 h over the ridge top.

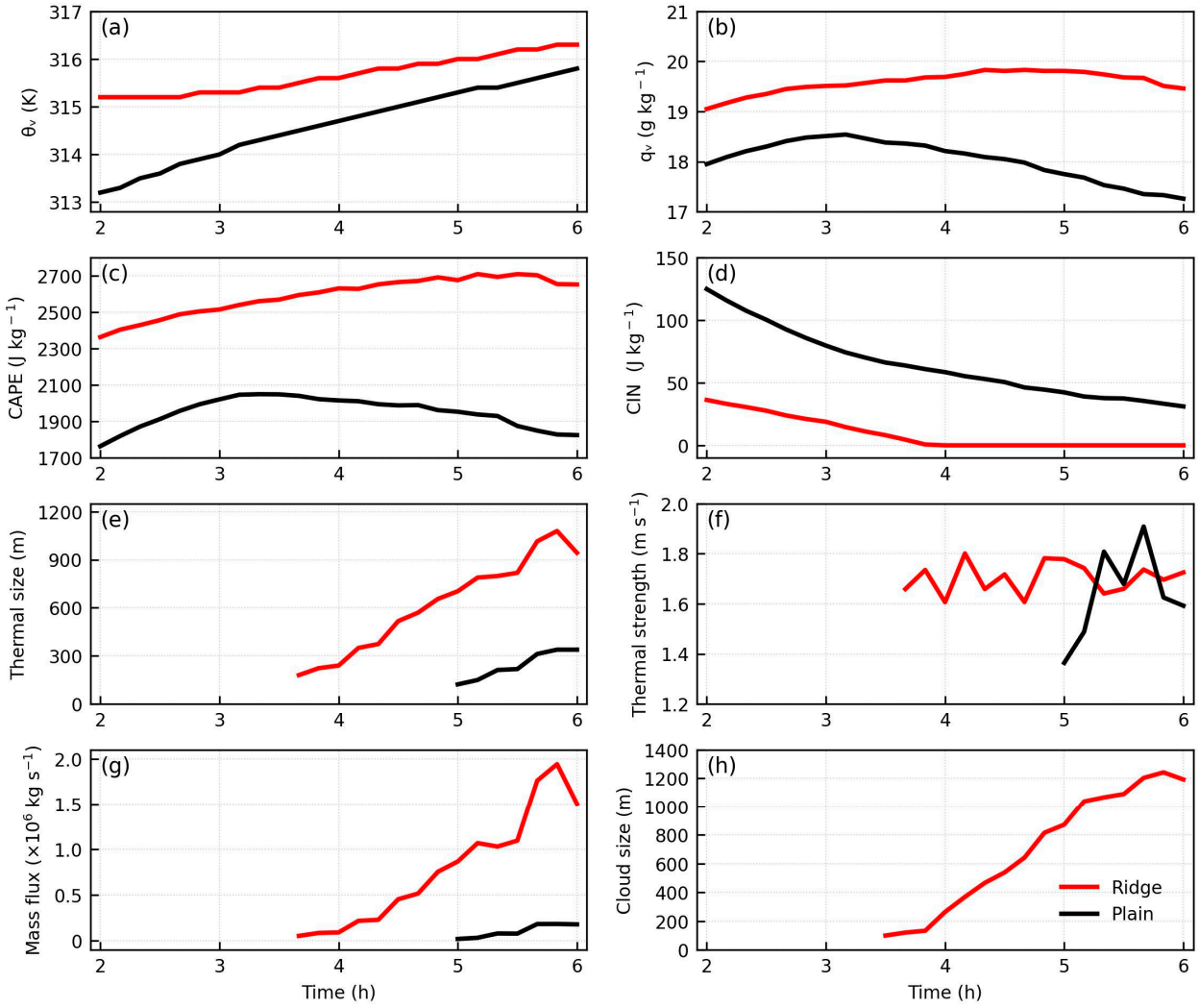

Figure 6. Temporal evolutions of (**a**) virtual potential temperature, (**b**) vapor mixing ratio, (**c**) CAPE, (**d**) CIN, (**e**) size of the composite thermal, (**f**) mean vertical velocity of the composite thermal, (**g**) mass flux of the composite thermal, and (**h**) mean size of SCCs in Simulation 2DX_1500. Virtual potential temperature and vapor mixing ratio were calculated at the middle of the CBL and averaged along the *y*-direction.

Thermals start to form at t = 3.5 h over the ridge top and t = 5 h over the plains. Actually, thermals do form in the earlier times, but these are not strong enough to be included in the compositing procedure. The size of the composite thermal increases with time, both over the ridge top and over the plain (Figure 6e). Thermal size scales with the depth of the CBL, which is forced to increase with time by the surface sensible heat flux. Over the ridge top, the convergence of the upslope winds increases the thermal size over the ridge top, while no such convergence exists over the plain. As a result, the thermal is larger over the ridge top than over the plain. The vertical velocity of the thermals over the ridge top is similar to that over the plain and is quasi-constant (Figure 6f). The evolution of the mass flux of the composite thermal generally follows the evolution of the size of the composite thermal (Figure 6g), so the mass flux of the composite thermal over the ridge is also larger than that over the plain near the end of the simulation.

SCCs develop over the ridge (Figure 6h), as a result of the large CAPE, negligible CIN, and large thermal. Cloud size also increases with time. Comparing the evolution of cloud size to the evolutions of CAPE, CIN, and thermal size, it is clear that the increase in cloud size is mainly due to the increase in thermal size. Over the plains, the thermals are so weak

that they cannot overcome the negative impacts of the large CIN and low humidity. As a result, SCCs do not develop over the plains.

The impacts of increasing the half-width of the isolated ridge are shown in Figure 7. Increasing the half-width slightly increases the temperature (Figure 7a) and humidity (Figure 7b), and therefore, slightly increases CAPE (Figure 7c) over the ridge top. CIN is negligible over the ridge top in all three 2DX simulations (Figure 7d). The impact on the strength of the composite thermal is also very small (Figure 7f). However, increasing the half-width substantially increases the size of the composite thermal (Figure 7e) and, therefore, the associated mass flux (Figure 7g). As a result, the cloud size also increases substantially (Figure 7h). Over the plains, CAPE is smaller, CIN is larger, and the thermals are smaller and weaker, so that no SCC forms.

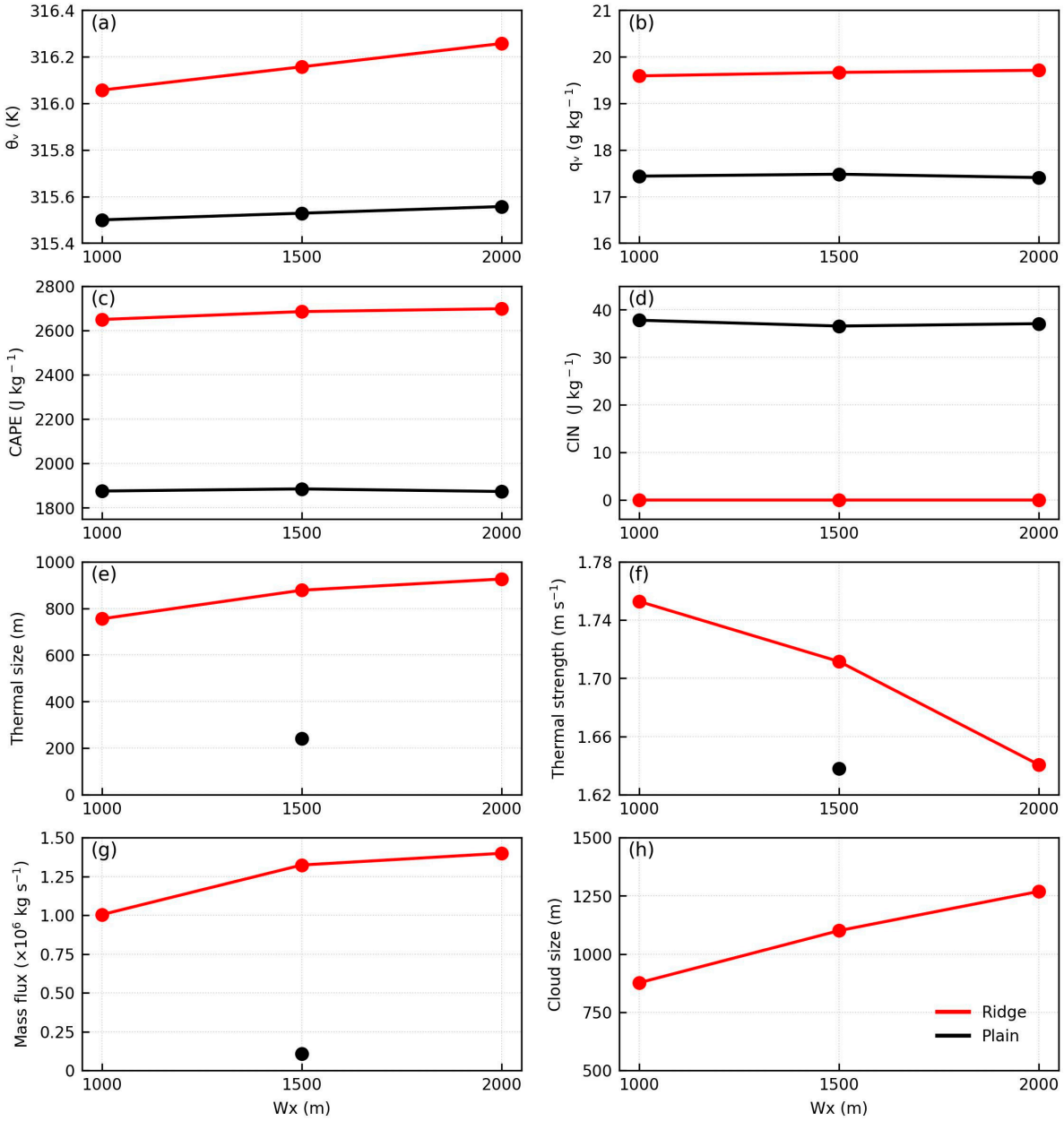

Figure 7. (**a**) Virtual potential temperature, (**b**) vapor mixing ratio, (**c**) CAPE, (**d**) CIN, (**e**) size of the composite thermal, (**f**) mean vertical velocity of the composite thermal, (**g**) mass flux of the composite thermal, and (**h**) mean size of SCCs. The values were averaged from t = 5 to 6 h and for the 2DX simulations. Compositing was not performed over the plains of Simulations 2DX_1000 and 2DX_2000 because the numbers of thermals are not sufficient.

3.2. 2DY Simulations

We now turn to the 2DY simulations. Figure 8 shows the temperature, humidity, wind in the y-direction (v-wind), CAPE, and CIN of Simulation 2DY_3000. The temperature is higher over the ridge top than over the valley at the same height (Figure 8a), leading to the formation of upslope winds (Figure 8c). Due to the vapor transport by the upslope winds, humidity reaches maxima over the ridge tops (Figure 8b). CAPE reaches maxima and CIN reaches minima over the ridge tops (Figure 8d,e). Return flows are seen above the upslope flows, and extend from the upper CBL to above the CBL (Figure 8c). When the air in the return flows moves from the ridge toward the valley, it mixes with the dry air above the CBL, gradually decreasing its humidity. When the return flows from neighboring ridges collide, the dry air sinks toward the surface, resulting in the humidity being lowest over the valley. Compared to the environments over the ridge tops, the environments over the valleys are less favorable for the formation of SCCs, as revealed by the smaller CAPE and larger CIN.

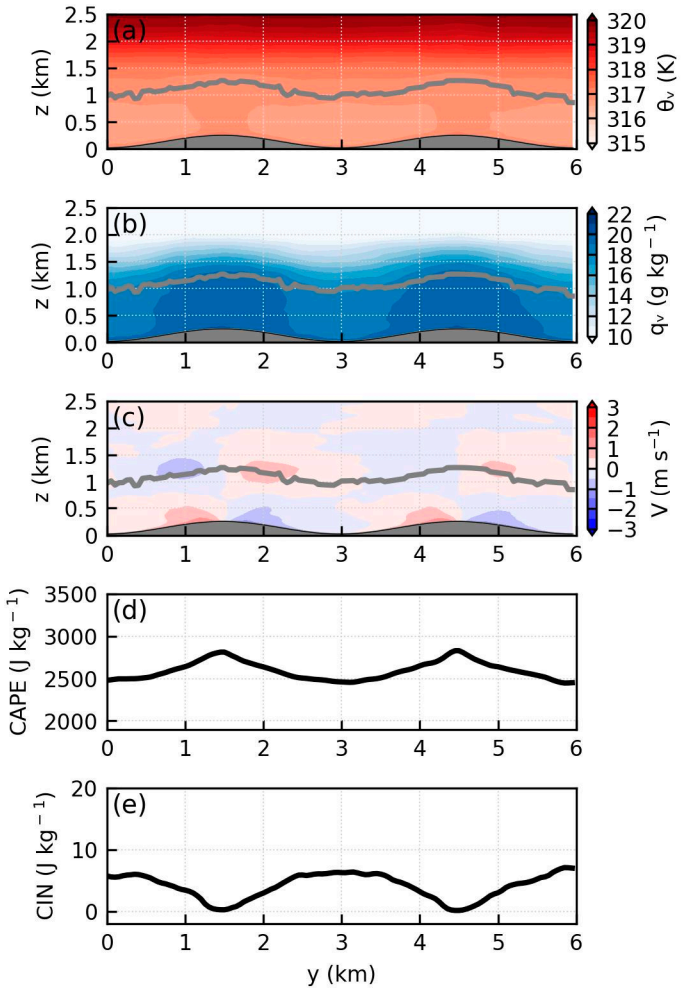

Figure 8. x-averaged (**a**) virtual potential temperature, (**b**) vapor mixing ratio, (**c**) v-wind, (**d**) CAPE, and (**e**) CIN at t = 6 h of Simulation 2DY_3000. The gray lines in (**a**–**c**) indicate the top of the convective boundary layer. Only two ridges are shown for clarity.

The properties of the composite thermals of Simulation 2DY_3000 are shown in Figure 9. For the 2DY simulations, the ridges are defined as the regions with $f_y > 0.5$, and the rest of the regions are defined as valleys. A thermal is defined as over the ridge if its centroid is over the ridge, and over the valley if its centroid is over the valley. Compared to that over the valley, the composite thermal over the ridge has a larger size and a higher

humidity. Their temperatures are similar. It is thus obvious that the thermals over the ridge have a stronger capability of producing clouds.

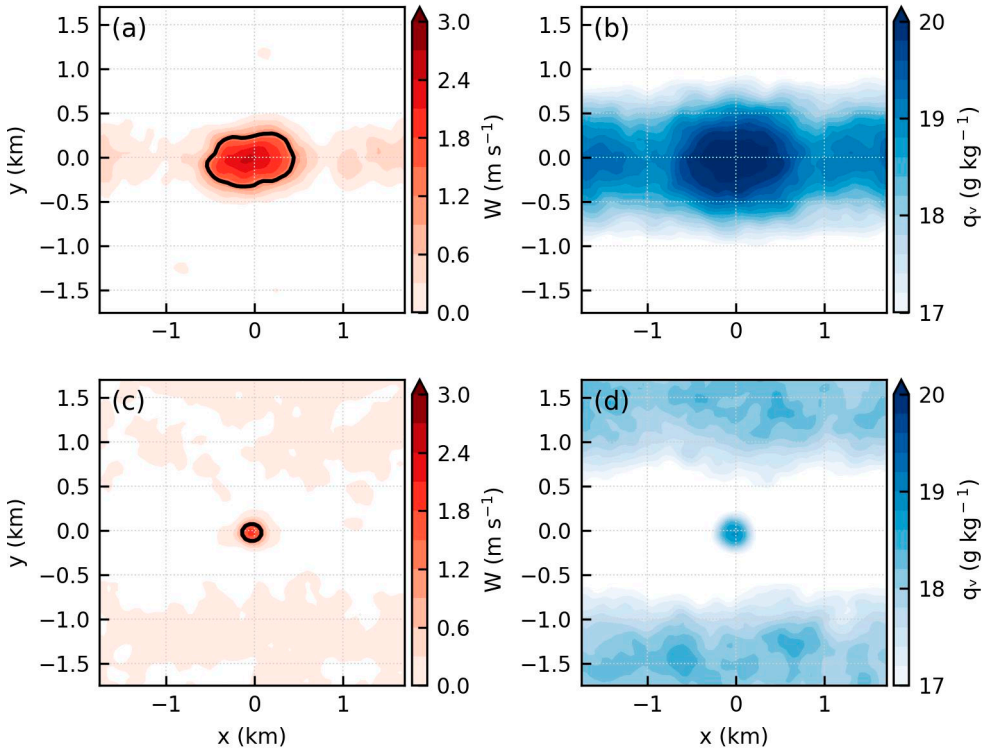

Figure 9. Properties of the composite thermals for Simulation 2DY_3000 from t = 5 to 6 h. (**a**) Vertical velocity, (**b**) vapor mixing ratio of the composite thermal over the ridges. The black line in (**a**) indicates the isoline of 1.2 m s^{-1}. (**c**,**d**) Same as (**a**,**b**) except for the composite thermal over the valleys.

The temporal evolutions of temperature, humidity, CAPE, and CIN in Simulation 2DY_3000 are generally similar to those in Simulation 2DX_1500 (cf. Figures 6 and 10). The size of the composite thermal also increases with time, both over the ridges and over the valleys (Figure 10e), due to the deepening of the CBL. More importantly, the composite thermal over the ridges has a larger size and a stronger vertical velocity than that over the valleys (Figure 10e,f). Over the ridge, the convergence of the upslope flows in the lower CBL enhances the development of thermals. Over the valley, however, the convergence of the return flows near the top of the CBL suppresses the development of thermals. The mass flux of the composite thermal is much larger over the ridges than over the valleys (Figure 10g). As a result, SCCs form earlier and are much bigger over the ridges (Figure 10h).

The impacts of increasing W_y are shown in Figure 11. Temperature increases with W_y over the ridge and decreases with W_y over the valley. However, note that the temperature change is very small (Figure 11a). Increasing W_y increases humidity over the ridge top and decreases humidity over the valley (Figure 11b). Upslope winds develop in all 2DY simulations. In the simulations with larger W_y, upslope winds cover a longer distance, so more vapor is collected as the air moves toward the ridge tops, resulting in higher humidity over the ridge top. Similarly, the return flows also cover longer distances, so more dry air is mixed into the return flows. Consequently, the humidity over the valley decreases with W_y. CAPE increases with W_y over the ridge and decreases with W_y over the valley (Figure 11c), similar to the response of humidity to W_y. CIN is negligible over the ridges for all 2DY simulations and is not negligible over the valley when $W_y \geq 3000$ m (Figure 11d).

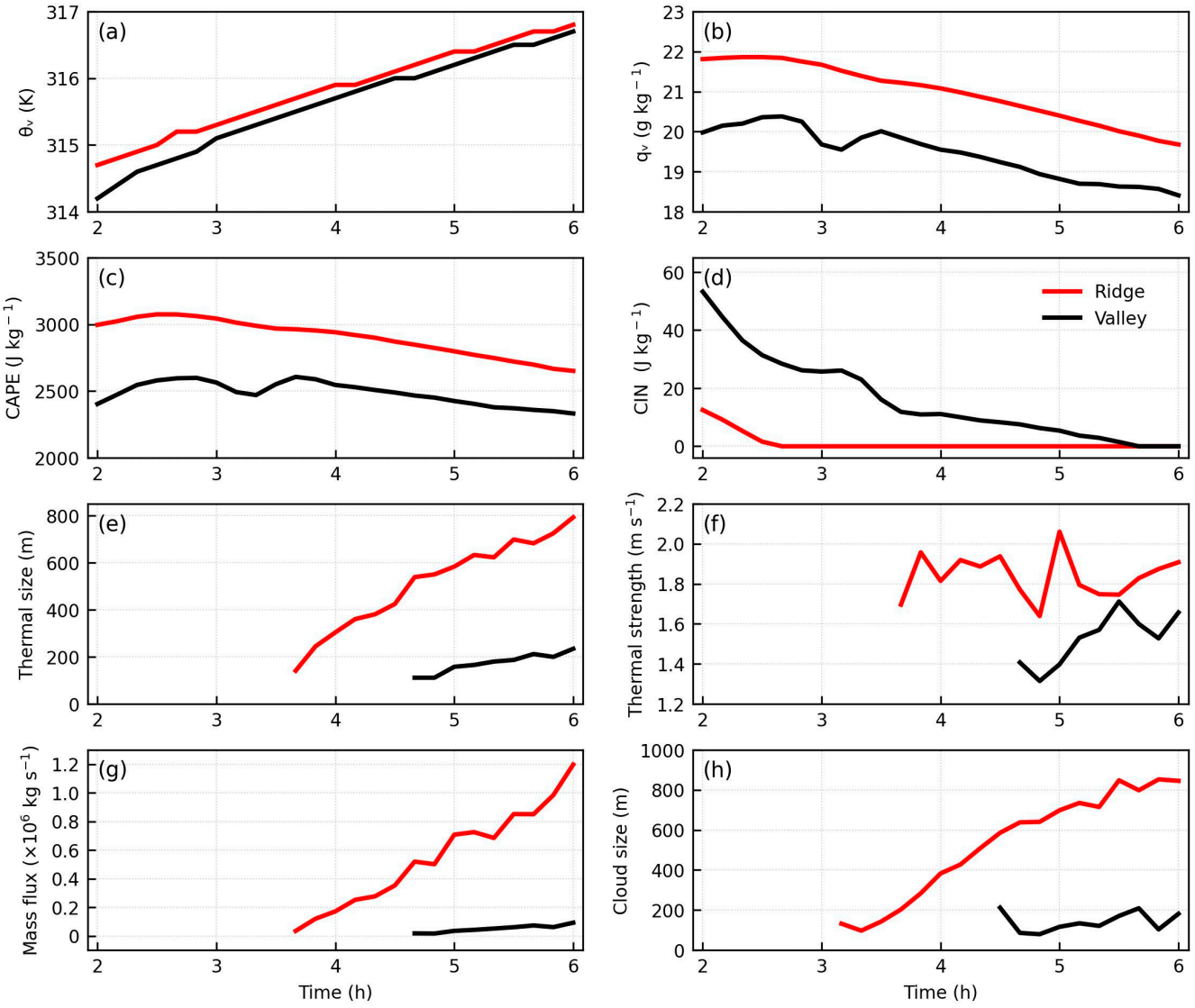

Figure 10. Temporal evolutions of (**a**) virtual potential temperature, (**b**) vapor mixing ratio, (**c**) CAPE, (**d**) CIN, (**e**) size of the composite thermal, (**f**) mean vertical velocity of the composite thermal, (**g**) mass flux of the composite thermal, and (**h**) mean size of SCCs in Simulation 2DY_3000. Virtual potential temperature and vapor mixing ratio were calculated at the middle of the CBL and averaged along the *y*-direction.

The size of the composite thermal over the ridges increases with W_y (Figure 11e). When $W_y \leq 2200$ m, the distance between the neighboring ridges is limited so that the thermals do not have enough space to develop. The thermals become bigger when the distance between the neighboring ridges increases. When $W_y > 2200$ m, the increase in thermal size with W_y is mainly due to the enhanced convergence of upslope winds. The vertical velocity of the composite thermal over the ridge is larger than that over the valley (Figure 11f), because the convergence of upslope flows promotes the development of thermals, while the convergence of the return flows suppresses the development of thermals. The convergence of the return flows produces downdrafts over the valleys. The downdrafts become stronger when W_y is smaller because the downdrafts are constrained to smaller areas. It is expected that the vertical velocity of the updrafts becomes smaller as W_y decreases. However, the vertical velocity increased as W_y decreases from 2200 m to 1400 m. This is mainly because more of the updrafts that are produced over the ridges can move to the valleys due to the turbulent flows. The response of the mass flux of composite

thermals to W_y is similar to the response of the thermal size (Figure 11g). Due to the higher humidity and the larger thermals, clouds are bigger over the ridges than over the plains (Figure 11h). Furthermore, cloud size increases with W_y over the ridge. The increasing thermal size is the main contributor to the increase in cloud size, although the increasing CAPE might be another contributor.

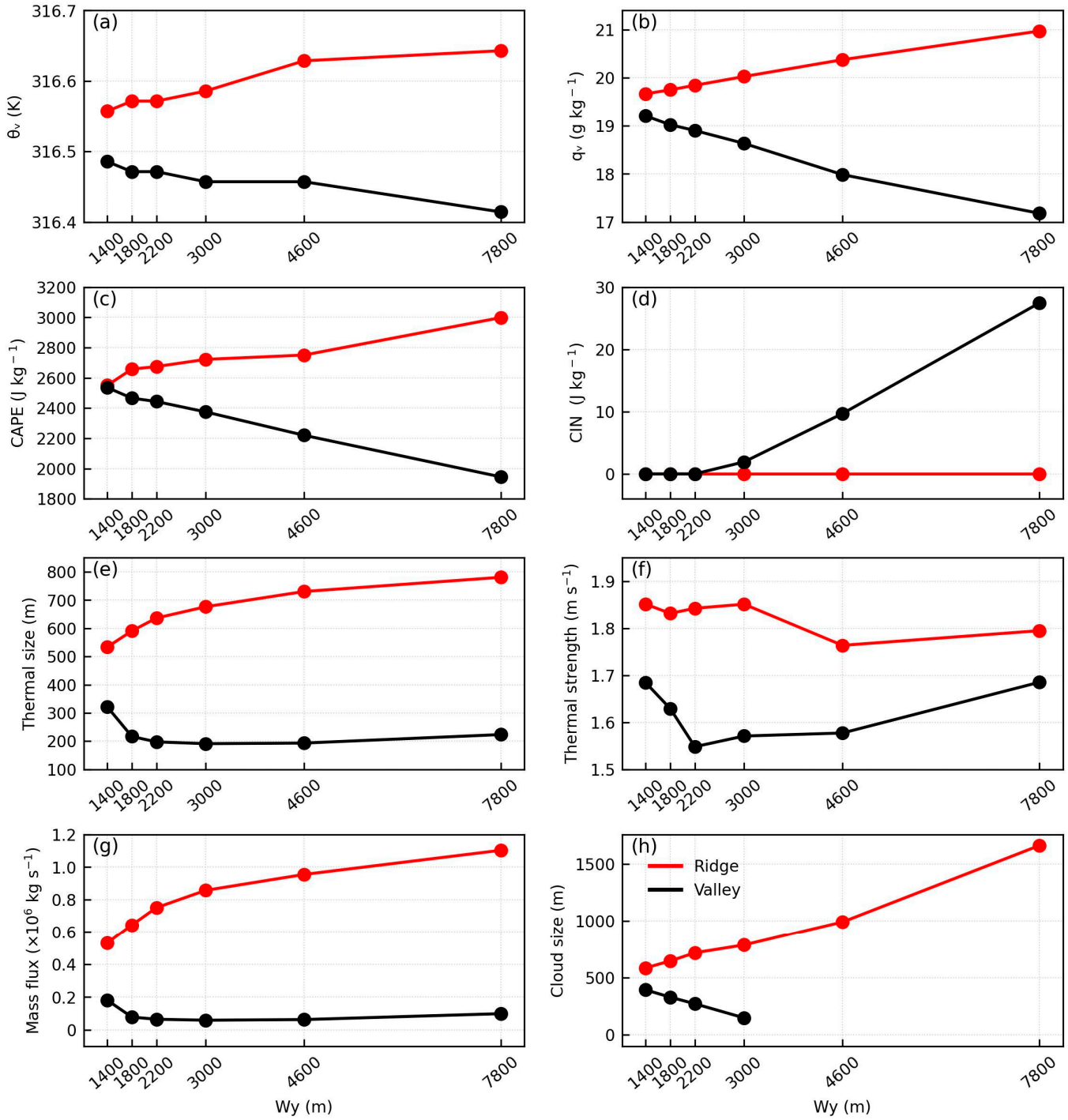

Figure 11. (**a**) Virtual potential temperature, (**b**) vapor mixing ratio, (**c**) CAPE, (**d**) CIN, (**e**) size of the composite thermal, (**f**) mean vertical velocity of the composite thermal, (**g**) mass flux of the composite thermal, and (**h**) mean size of SCCs averaged from t = 5 to 6 h of the 2DY simulations.

3.3. 3D Simulations

For the 3D simulations, simply averaging along the y-direction or x-direction is not appropriate. Therefore, we averaged the relevant variables over all minor ridges to get the mean fields. For a generic variable c, its average is

$$[c(x,y',z)] = \frac{1}{N}\sum_{n=0}^{N-1} c(x,y'+nW_y,z) \quad (7)$$

Here, N is the number of minor ridges, n is the corresponding index, and y' is the coordinate in the y-direction and takes values between 0 and W_y. Although $[c(x,y',z)]$ is defined between 0 and W_y in the y-direction, it is duplicated once when necessary, so the results are shown from 0 to $2W_y$. This makes the figures easier to interpret. In the 3D simulations, a slope exists both in the x-direction and in the y-direction, so slope flows develop in both directions. For clarity, the direction of the slope flow will be specified when discussing the results of the 3D simulations. Moreover, although minor valleys exist, typical valley winds are not produced in the simulations. In fact, the 3D topography used in this study does not resemble the typical topography that produces valley wind [52].

Figure 12 shows the averaged fields at the minor-ridge top and the minor-valley bottom. The results, either over the minor-ridge top or over the minor-valley bottom, are generally similar to those of the 2DX simulations (Figure 4). Moreover, Figure 12 further reveals that the upslope winds in the x-direction are much deeper over the minor-ridge top than over the minor-valley bottom, while the return flows are much shallower over the minor-ridge top than over the minor-valley bottom.

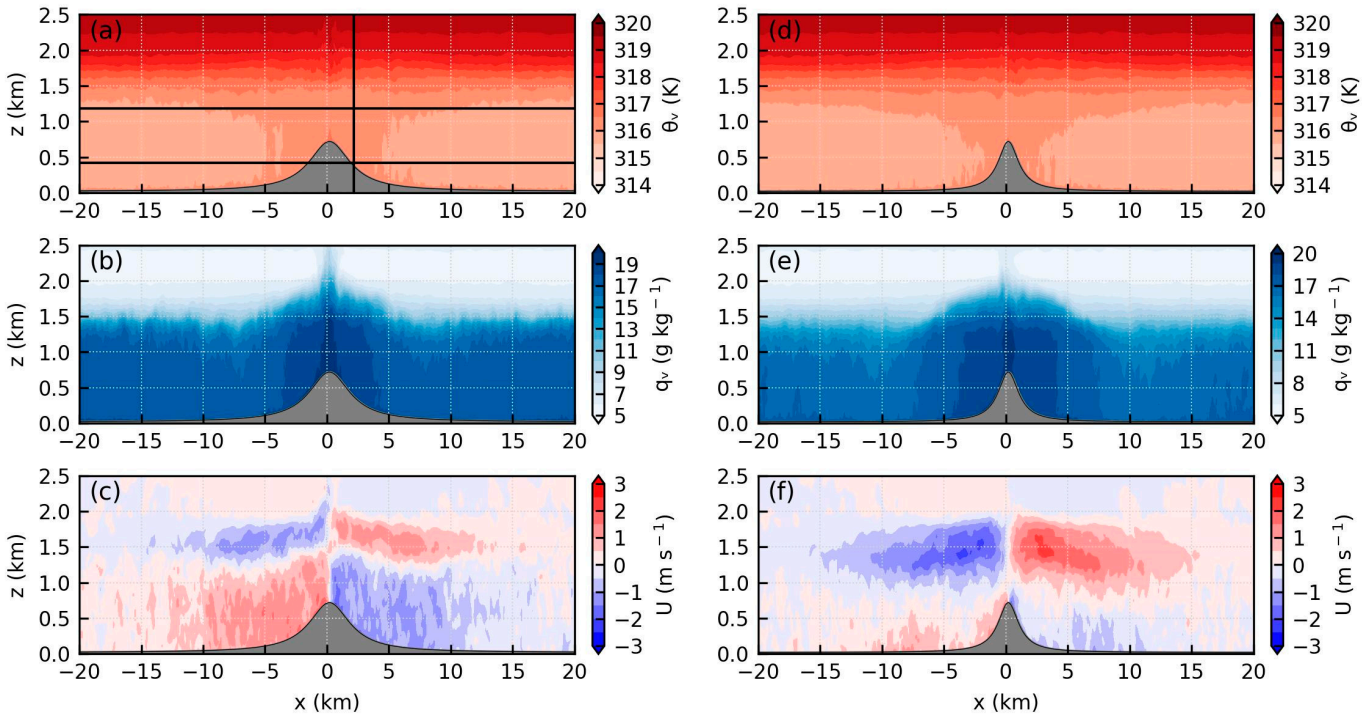

Figure 12. (**a**) Virtual potential temperature, (**b**) vapor mixing ratio, and (**c**) u-wind in the x-z plane averaged over all minor-ridge tops in Simulation 3D_3000. (**d**–**f**) Same as (**a**–**c**) except for the fields averaged over all minor-valley bottoms. The horizontal lines and the vertical line in (**a**) indicate the positions where the horizontal cross-sections and vertical cross-section are shown later, respectively.

On a horizontal plane at z = 420 m (Figure 13a–d), the upslope flows in the x-direction are prominent over the minor ridges and are negligible over the minor valleys (Figure 13c). Upslope flows in the y-direction are clearly visible at z = 420 m (Figure 13d). Their con-

vergences produce updrafts over the minor ridges. At z = 1180 m (Figure 13e–h), upslope flows in the x-direction are only seen in small regions where the major ridge and the minor ridges intersect (Figure 13g). Return flows in the x-direction are prominent over the minor valleys. Return flows in the y-direction also develop (Figure 13h).

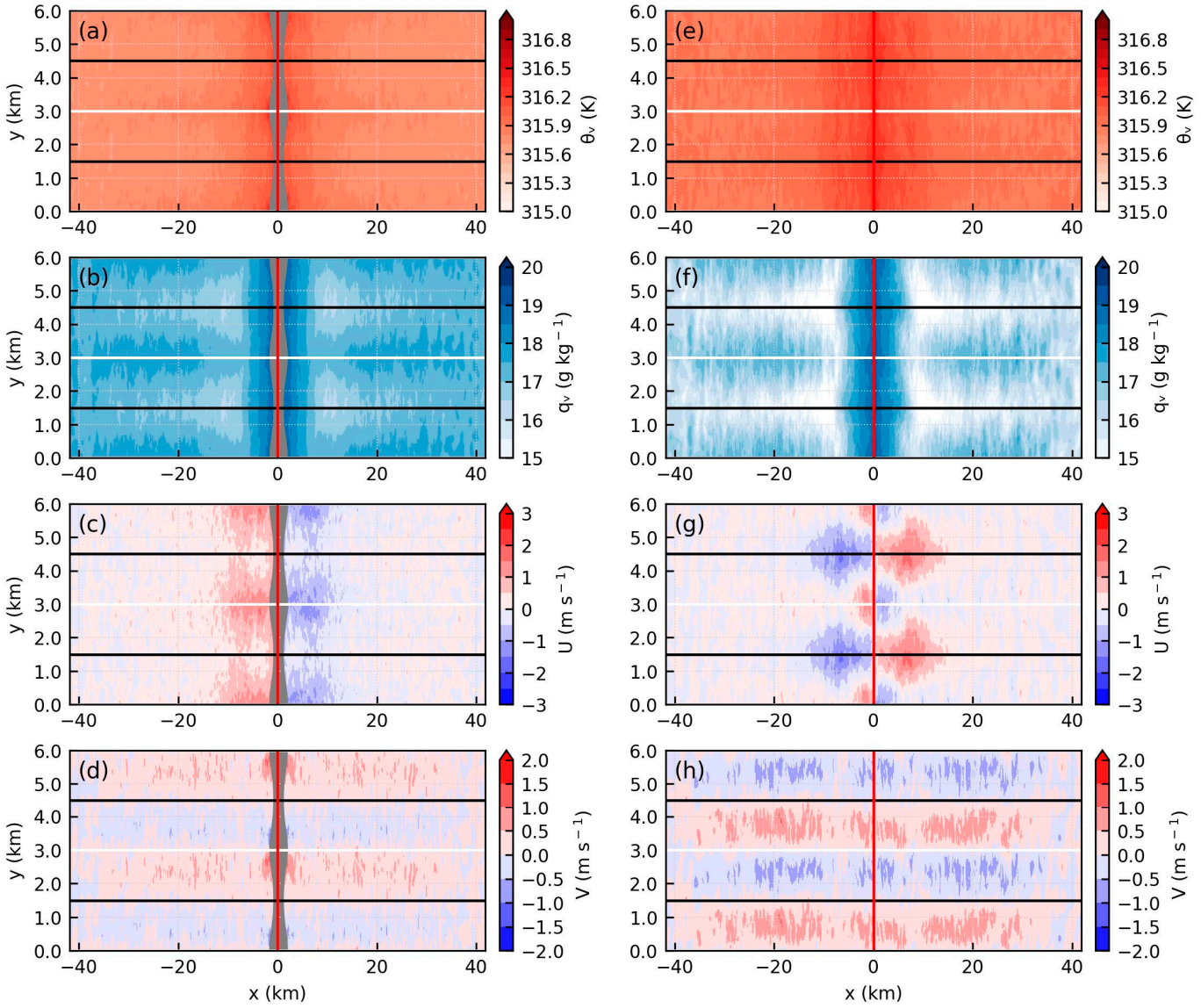

Figure 13. (**a**) Virtual potential temperature, (**b**) vapor mixing ratio, (**c**) u-wind, and (**d**) v-wind in a horizontal plane at z = 420 m (the lower solid line in Figure 12a) in Simulation 3D_3000. (**e**–**h**) Same as (**a**–**c**) except for a horizontal plane at z = 1180 m (the upper solid line in Figure 12a). The red lines, white lines, and black lines indicate the major ridge, minor ridges, and minor valleys, respectively. The results are averaged over all minor ridges. Note that the averaged results are defined over the domain with a length of W_y in the y-direction, but it is duplicated here, so the displayed domain has a length of $2W_y$ in the y-direction.

Figure 14 shows a vertical plane at x = 2 km. It shows that upslope flow and return flow in the x-direction are spatially staggered in the y-direction (Figure 14c); i.e., the upslope flows are mainly over the minor ridges and the return flows are mainly over the minor valleys. The upslope flows and the associated return flows in the y-direction are also visible in Figure 14d.

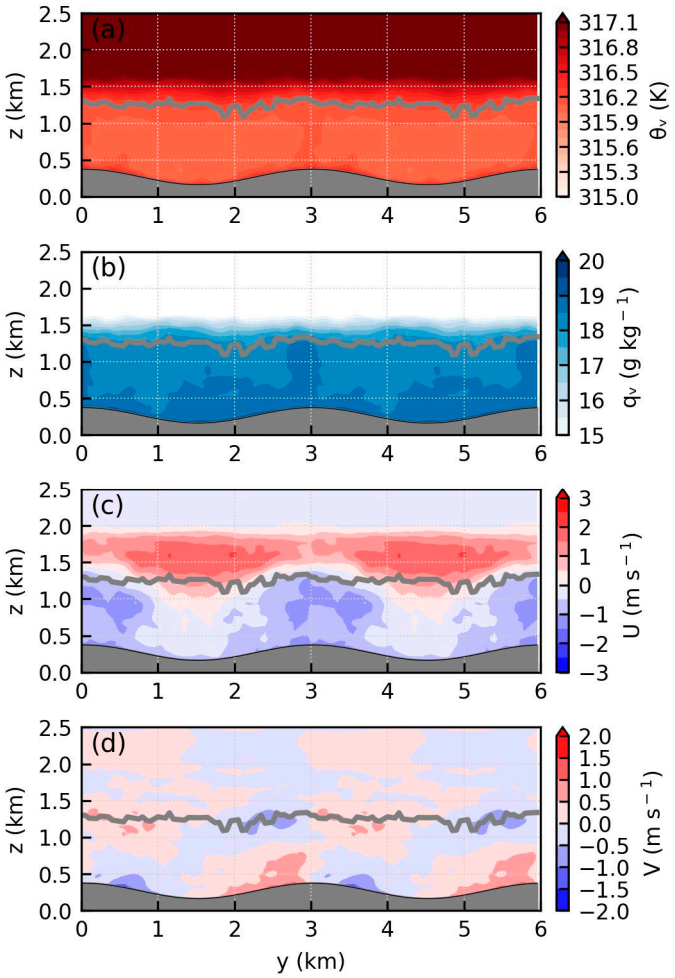

Figure 14. (**a**) Virtual potential temperature, (**b**) vapor mixing ratio, (**c**) u-wind, and (**d**) v-wind in a y-z plane at x = 2 km (the vertical line in Figure 12a) in Simulation 3D_3000. The results are averaged over all minor ridges. The gray lines indicate the top of the convective boundary layer. Note that the averaged results are defined over the domain with a length of W_y in the y-direction, but it is duplicated here, so the displayed domain has a length of $2W_y$ in the y-direction.

In the x-direction, the humidity was highest over the major ridge (Figures 12 and 13), because of the vapor transport by the upslope flows in the x-direction. We now focus on the variation in humidity in the y-direction over the major ridge. Near the surface, the upslope flows in the y-direction also transport vapor toward the minor ridge top. This tends to increase the humidity over the minor-ridge top and decrease the near-surface humidity over the minor-valley bottom, as can be seen from Figure 13b. However, this was further complicated by the process near the CBL top. The high-humidity air is transported from the minor ridges toward the minor valleys by the return flows in the y-direction (Figure 13h), and is concurrently transported away from the major ridges by the return flows in the x-direction (Figure 13g). Consequently, the humidity at the CBL top is increased over the minor valleys (Figure 13f). When this humid air is entrained into the CBL, the near-surface humidity over the minor valleys is also increased. The competition between the processes near the surface, which tends to decrease humidity over the minor valleys, and the processes near the CBL top, which tends to increase humidity over the minor valleys, determines whether the humidity is higher over the minor ridges or over the minor valleys. In Simulation 3D_3000, the humidity over the minor ridges is slightly higher than that over the minor valleys (Figure 14b). The opposite result also occurs, as shown later.

The size of the composite thermal is much larger over the ridge than over the valley (Figure 15a,c), due to the convergences both in the x-direction and in the y-direction. Note that Figure 15 shows the result of the simulation with W_y = 3000 m. In this simulation, the distances between the valley and the neighboring ridges are 1.5 km. In Figure 15c, the thermal at y = 0 km is over the valley, while the thermals at $y = \pm 1.5$ km are over the neighboring ridges. The humidity over the ridge is close to that over the valley (Figure 15b,d). As explained earlier, although the vapor transport by the upslope flows in the x-direction is mainly over the minor ridges, the vapor transport by the return flows in the y-direction can also increase the humidity over the minor valleys. Thus, the humidity over the minor ridges is only slightly higher than that over the minor valleys. The temperature difference is also negligible, similar to the 2DX simulations.

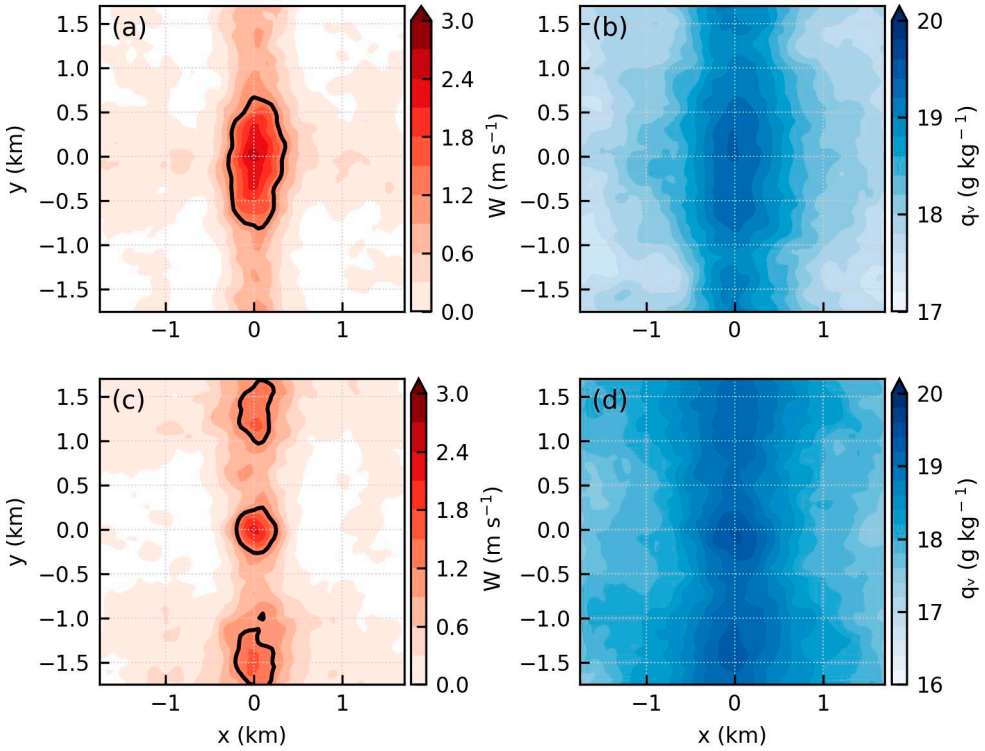

Figure 15. Properties of the composite thermals for Simulation 3D_3000 from t = 5 to 6 h. (**a**) Vertical velocity, (**b**) vapor mixing ratio of the composite thermal over the minor ridges. The black line in (**a**) indicates the isoline of 1.2 m s^{-1}. (**c**,**d**) Same as (**a**,**b**) except for the composite thermal over the minor valleys.

We now analyze the temporal evolutions of temperature, humidity, CAPE, and CIN. In Figure 16a–d, the minor ridges refer to the positions with x = 0 and f_y = 1, and the minor valleys refer to the positions with x = 0 and f_y = 0. In fact, at x = 0, the terrain height equals H_m for any y. However, as shown later, the positions connected to the minor ridges have different characteristics from the positions connected to the minor valleys, so it is still useful to define minor ridges and minor valleys at x = 0. Temperature increases with time both over the minor ridges and over the minor valleys (Figure 16a). Humidity is initially higher over the minor ridges than over the minor valleys, with a difference of around 1 g kg^{-1} at t = 2 h (Figure 16b). This is because the upslope flows in the y-direction transported vapor from the minor valleys to the minor ridges. In the later times, the return flows in the y-direction gradually transport vapor toward the minor valleys, and thereby increase the humidity over the minor valleys. As a result, the humidity difference gradually decreases with time. CAPE over the ridge top is quasi-constant from t = 2 to 6 h (Figure 16c),

indicating that the effect of increasing temperature counteracts the effect of decreasing humidity. CAPE over the valley bottom increases with time, especially between t = 2 to 4 h, closely following the evolution of humidity. CIN decreases to zero both over the minor ridges and over the minor valleys (Figure 16d), similar to those in the 2DX simulations.

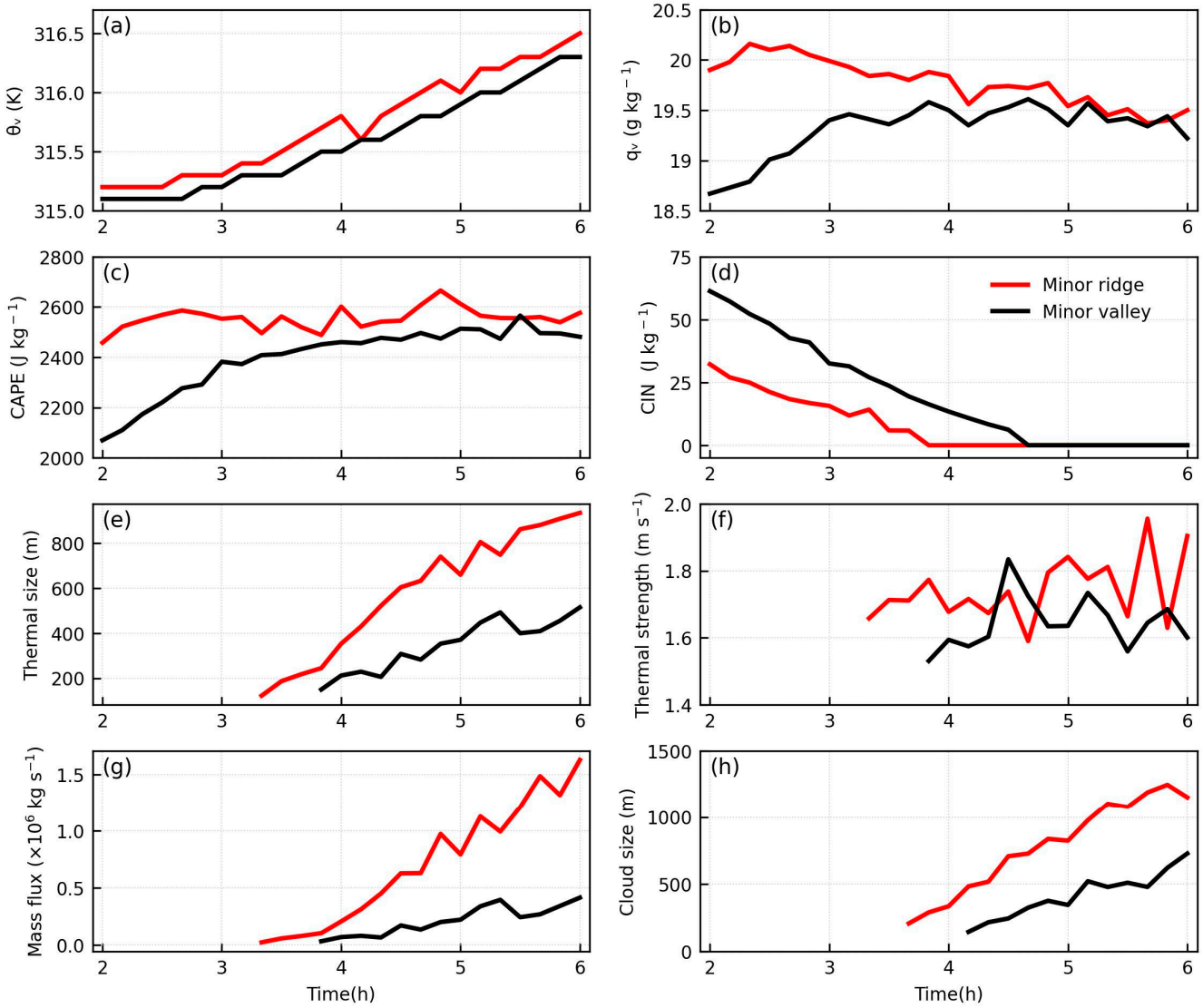

Figure 16. Temporal evolutions of (**a**) virtual potential temperature, (**b**) vapor mixing ratio, (**c**) CAPE, (**d**) CIN, (**e**) size of the composite thermal, (**f**) mean vertical velocity of the composite thermal, (**g**) mass flux of the composite thermal, and (**h**) mean size of SCCs in Simulation 3D_3000. Virtual potential temperature and vapor mixing ratio were calculated at the middle of the CBL and averaged along the *y*-direction.

Thermals start to form around t = 3.5 h and their sizes increase with time (Figure 16e), similar to those in 2DX and 2DY simulations. The convergence provided by the upslope flows in the *x*-direction is much stronger over the minor ridges than over the minor valleys (Figures 12 and 13), so the composite thermal over the minor ridges is much larger than that over the minor valleys. This is slightly different from those in the 2DY simulations. In the 3D simulations, the upslope flows in the *y*-direction affect the thermal size by forcing the upslope flows in the *x*-direction to be over the minor ridges. It is the upslope flows in the *x*-direction that directly enlarge the thermals over the minor ridges. In the 2DY simulations, it is the upslope flows in the *y*-direction that directly enlarge the thermals. The vertical velocity of the composite thermal over the minor ridge is similar to that over the

minor valley (Figure 16f). This is different from the 2DY simulations. In 3D simulations, the circulations in the y-direction are weak over the ridge top, so they cannot enhance or suppress the development of thermals. In the 2DY simulations, the local circulation in the y-direction is strong, so the vertical velocity over the ridges is enhanced and the vertical velocity over the valleys is suppressed. The evolution of the mass flux is dominated by that of the thermal size (Figure 16g). The cloud size over the minor ridges is much larger than that over the minor valleys (Figure 16h). It is clear that the cloud size is predominantly determined by the thermal size, as also seen in the 2DX and 2DY simulations.

The impacts of increasing W_y in the 3D simulations are shown in Figure 17. The temperature difference is small between the minor ridges and the minor valleys (Figure 17a), similar to that in the 2DX and 2DY simulations. The humidity over the minor ridge is close to that over the minor valleys (Figure 17b). This is different from the 2DY simulations, where the humidity over the minor ridges is substantially higher than over the minor valleys (cf. Figure 11b). As explained earlier, the return flows in the y-direction tend to increase the humidity over the minor valleys, so the humidity difference is substantially reduced. It is interesting to note that the humidity over the minor ridge is slightly lower than over the minor valley in Simulation 3D_4600. In this simulation, the vapor transport by the upslope flows in the y-direction is weak, so a negligible amount of vapor is transported from the minor valley toward the minor ridge near the surface, while the return flows in the y-direction are prominent, so vapor is transported from the minor ridge toward the minor valley near the CBL. The response of CAPE to increasing W_y is similar to that of humidity (Figure 17c). CIN is negligible, both over the minor ridges and over the minor valleys (Figure 17d).

We now analyze the impacts of varying W_y on thermal sizes (Figure 17e). When W_y is infinitely large, the local topography over the minor ridges becomes similar to that of Simulation 2DX_2000, and the local topography over the minor valleys becomes similar to that of Simulation 2DX_1000. Note that the half-width in the x-direction in the 3D simulations is 2000 m at the minor ridge and is 1000 m at the minor valley (Section 2.3). In this situation, thermal size over the minor ridges is expected to be similar to that of Simulation 2DX_2000, and the thermal size over the minor valleys is expected to be similar to that of Simulation 2DX_1000. A comparison of Figures 7e and 17e reveals that the thermal size over the minor valley of Simulation 3D_7800 is close to that over the ridge of Simulation 2DX_1000, while the thermal size over the minor ridge of Simulation 3D_7800 is larger than that over the ridge of Simulation 2DX_2000. The discrepancy may arise from the fact that 7800 m is not sufficiently large to be considered as infinity. Nevertheless, the thermal size is much larger over the minor ridge than over the minor valley, consistent with the 2DX simulations. When W_y becomes smaller, the circulation in the y-direction confines the upslope flows in the x-direction to the minor ridges, so the convergence in the x-direction is also confined to the minor ridges. Previous studies have shown that it was the convergence that produced the large updrafts [9,51]. When the spatial extent of convergence is confined, the size of the thermal is also confined. Consequently, thermal size decreases as W_y decreases, similar to that in the 2DY simulations.

In Simulation 3D_7800, the vertical velocity of the thermal over the minor ridge is similar to that over the minor valley (Figure 17f). When W_y becomes smaller, the local circulation acts to increase the vertical velocity of thermal over the minor ridges and decrease the vertical velocity of thermal over the minor valleys, similar to those in the 2DY simulations (cf. Figures 11f and 17f).

The impacts of varying W_y on the mass flux of thermals are still dominated by the change in thermal size (Figure 17g). Specifically, the mass flux over the minor ridges is larger than that over the minor valleys, and decreasing W_y decreases the mass flux both

over the minor ridges and over the minor valleys. Cloud sizes over the minor ridges are larger than those over the minor valleys (Figure 17h). Decreasing W_y decreases the cloud size. However, this trend is violated by clouds over the minor valleys when $W_y < 2000$. When W_y is small, it becomes difficult to unambiguously identify whether a cloud is over minor ridges or over minor valleys.

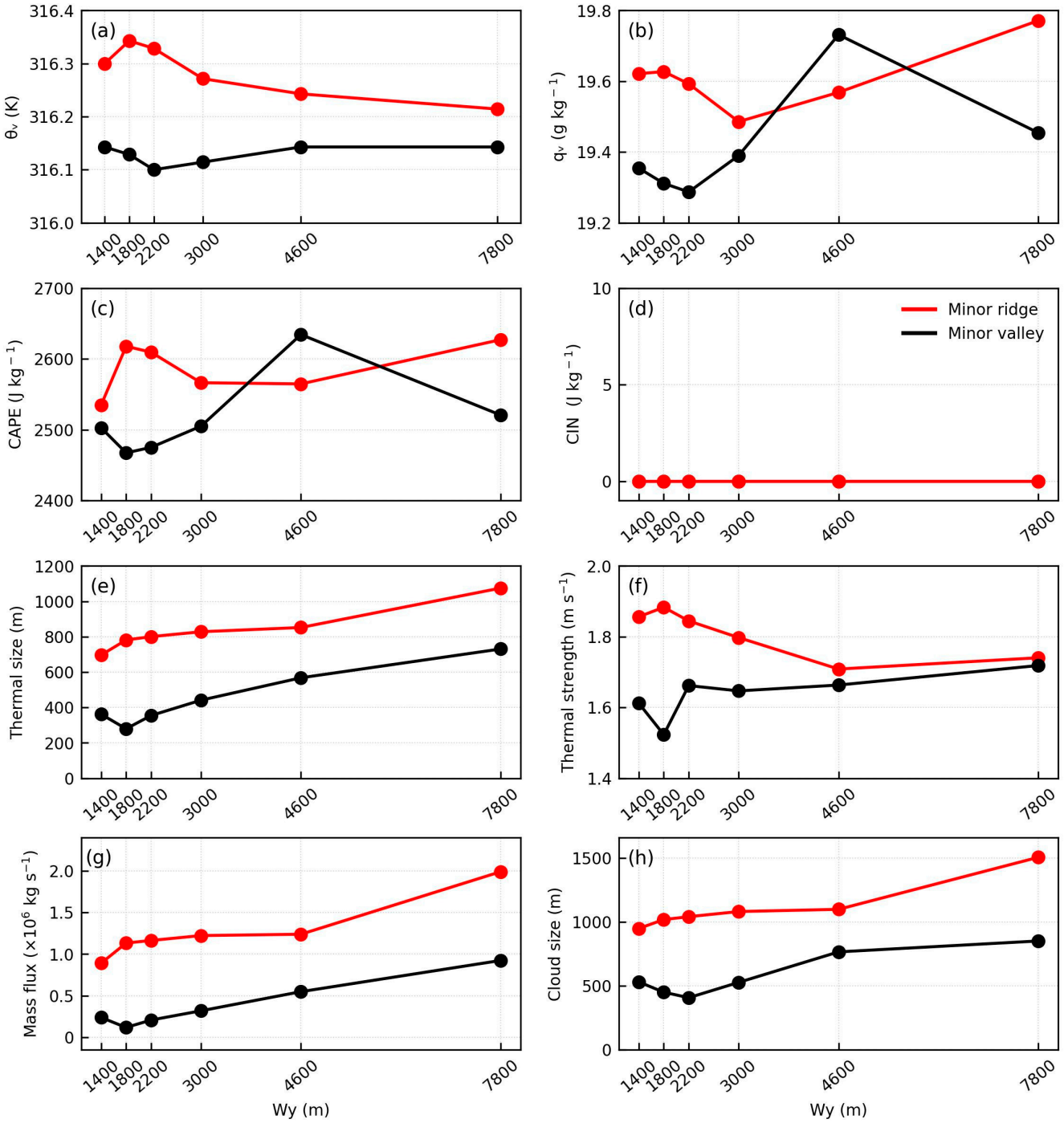

Figure 17. (**a**) Virtual potential temperature, (**b**) vapor mixing ratio, (**c**) CAPE, (**d**) CIN, (**e**) size of the composite thermal, (**f**) mean vertical velocity of the composite thermal, (**g**) mass flux of the composite thermal, and (**h**) mean size of SCCs averaged from t = 5 to 6 h of the 3D simulations. Note that the two lines overlap in (**d**).

3.4. Discussion

A good linear relation between the size of the cloud and the size of the composite thermal is seen when all three sets of simulations are taken together (Figure 18a), suggesting that this relation is robust even when the underlying topography is different. The fitted line is $y = 1.3\ x$, with a correlation coefficient $R^2 = 0.99$. We forced the line to pass the origin because no cloud should exist when no thermal exists. Note that the outliers, i.e., SCCs over the ridge of Simulation 2DY_7800, were excluded from the fitting. In this simulation, the humidity is very high over the ridges (Figure 11b). The clouds are so big that some of them connect with their neighbors and cannot be separated by our simple cloud identification method, so the clouds are abnormally large. Additionally, no SCC develops over the valleys of Simulations 2DY_4600 and 2DY_7800, because the thermals are very small and the humidity is very low (Figure 11). These two scenarios were also excluded from the fitting.

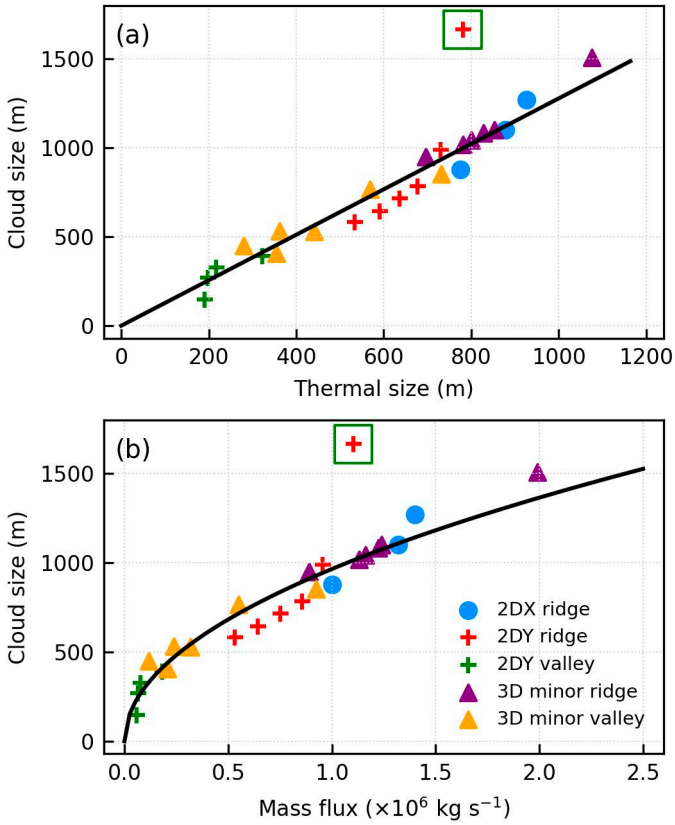

Figure 18. The relationship between cloud size and the (**a**) size of the composite thermal and (**b**) mass flux of the composite thermal. The outlier is marked with a green box. The black lines in (**a**) and (**b**) show the fitted results $y = 1.3\ x$ and $y = 964\ \sqrt{x}$, respectively.

A good relationship is also seen between the cloud size and the mass flux of the composite thermal (Figure 18b). It is well-fitted by the function $y = 964\sqrt{x}$, with $R^2 = 0.95$. The mass flux (F) is related to the thermal size via $F = \bar{w} {l_{thermal}}^2$, where $\overline{w}$ is the mean vertical velocity of the thermal, and $l_{thermal}$ is the size of the thermal. In our simulations, the mean vertical velocities of the composite thermals are close to each other. As a result, the linear relation between the size of the cloud and the size of the composite thermal directly leads to the square-root relation between the size of the cloud and the mass flux of the composite thermal. More simulations with different setups, e.g., initial conditions and surface heat fluxes, are necessary to further test these two relations.

4. Conclusions

Large-eddy simulations (LESs) were performed to investigate how three-dimensional (3D) topography affected shallow-convective clouds (SCCs). The 3D topography was constructed using two widely used two-dimensional (2D) topographies. The first is a bell-shaped ridge that varies in the x-direction only. The second is a series of sinusoidal ridges that vary in the y-direction only. The bell-shaped ridge is the major ridge, which is attached to the minor ridges and minor valleys of the sinusoidal topography. The wavelength of the sinusoidal ridges is systematically varied to investigate the responses of the SCCs. In order to better understand the underlying mechanisms, LESs were also performed separately using the two types of 2D topography.

In the simulations using the 2D bell-shaped topography, the formation of upslope winds produces larger thermals and higher humidity over the ridge top than over the plains, so that SCCs develop over the ridge, and increasing half-width increases the size of SCCs. The impacts of the 2D bell-shaped topography on SCCs are consistent with the existing research results [33]. In the simulations using 2D sinusoidal topography, upslope winds and return flows also develop, promoting the formation of SCCs over the ridges and suppressing the formation of SCCs over the valleys, and increasing the wavelength increases the size of SCCs over the ridges and decreases the size of SCCs over the valleys. In the simulations with 3D topography, the upslope winds are mainly over the minor ridges and the return flows are mainly over the minor valleys, due to the circulations produced by the minor ridges and minor valleys. This is different from the results obtained using 2D topographies, where the upslope winds and return flows are homogeneous along the ridge axes. The upslope winds also promote the development of SCCs over the major ridges by producing large thermals and high humidity, similar to the simulations using 2D topographies. Furthermore, thermals over the intersection points of the major ridge and the minor ridges are bigger than those over the intersection points of the major ridge and the minor valleys, so the SCCs are larger over the intersection points of the major ridge and the minor ridges. Increasing the wavelength of minor ridges increases the region with upslope winds. This increases the region with convergence and, therefore, increases the size of SCCs.

In previous studies of topographic impacts on clouds, it is common to use 2D topography. This study shows that the results obtained using 2D topography capture important aspects of topographic impacts on SCCs, e.g., the transport of vapor by upslope winds and the formation of large thermals by the convergence of upslope winds. Nevertheless, this study further reveals that the upslope flows and the return flows are more complex when 3D topography is considered, so the topographic impacts on SCCs are also more complex.

Author Contributions: Conceptualization, S.F.; methodology, Y.H. and S.F.; software, Y.H.; validation, Y.H., S.F. and X.D.; formal analysis, Y.H. and S.F.; investigation, Y.H. and S.F.; resources, S.F.; data curation, Y.H.; writing—original draft preparation, Y.H. and S.F.; writing—review and editing, S.F. and X.D.; visualization, Y.H. and M.G.; supervision, S.F.; project administration, S.F.; funding acquisition, S.F. All authors have read and agreed to the published version of the manuscript.

Funding: This research was supported by the National Natural Science Foundation of China (42105080) and the Special Fund for Science and Technology Innovation of Fujian Agriculture and Forestry University (KFB25059A). And the APC was funded by KFB25059A.

Institutional Review Board Statement: Not applicable.

Informed Consent Statement: Not applicable.

Data Availability Statement: The simulations were performed using Cloud Model 1 [53]. The sounding was obtained from University of Wyoming Atmospheric Science Radiosonde Archive [54]. The ERA5 data was obtained from ECMWF [55]. The data presented in this study are available on request from the corresponding author. The data are not publicly available due to privacy.

Acknowledgments: The simulations were run at the high-performance computing center of Fujian Normal University, and we hereby express our sincere gratitude for the computational resources and technical support provided by the center. Additionally, this research was supported by the National Natural Science Foundation of China (42105080), for which we extend our profound appreciation.

Conflicts of Interest: The authors declare no conflicts of interest.

References

1. Dror, T.; Koren, I.; Altaratz, O.; Heiblum, R.H. On the Abundance and Common Properties of Continental, Organized Shallow (Green) Clouds. *IEEE Trans. Geosci. Remote Sens.* **2021**, *59*, 4570–4578. [CrossRef]
2. Warren, S.G.; Hahn, C.J.; Julius, L. *Global Distribution of Total Cloud Cover and Cloud Type Amounts over Land*; U.S. National Center for Atmospheric Research: Boulder, CO, USA, 1986.
3. Warren, S.G.; Hahn, C.J.; Julius, L. *Global Distribution of Total Cloud Cover and Cloud Type Amounts over Ocean*; U.S. National Center for Atmospheric Research: Boulder, CO, USA, 1988.
4. Berg, L.K.; Kassianov, E.I.; Long, C.N.; Mills, D.L. Surface Summertime Radiative Forcing by Shallow Cumuli at the Atmospheric Radiation Measurement Southern Great Plains Site. *J. Geophys. Res.* **2011**, *116*, D01202. [CrossRef]
5. Savazzi, A.C.M.; Nuijens, L.; De Rooy, W.; Janssens, M.; Siebesma, A.P. Momentum Transport in Organized Shallow Cumulus Convection. *J. Atmos. Sci.* **2024**, *81*, 279–296. [CrossRef]
6. Larson, V.E.; Domke, S.; Griffin, B.M. Momentum Transport in Shallow Cumulus Clouds and Its Parameterization by Higher-Order Closure. *J. Adv. Model. Earth Syst.* **2019**, *11*, 3419–3442. [CrossRef]
7. Chen, G.; Xue, H.; Feingold, G.; Zhou, X. Vertical Transport of Pollutants by Shallow Cumuli from Large Eddy Simulations. *Atmos. Chem. Phys.* **2012**, *12*, 11319–11327. [CrossRef]
8. Kim, E.; Kim, B.U.; Kang, Y.H.; Kim, H.C.; Kim, S. Role of Vertical Advection and Diffusion in Long-range PM2.5 Transport in Northeast Asia. *Environ. Pollut.* **2023**, *320*, 120997. [CrossRef]
9. Fu, S.; Rotunno, R.; Chen, J.; Deng, X.; Xue, H. A Large-eddy Simulation Study of Deep-Convection Initiation Through the Collision of Two Sea-Breeze Fronts. *Atmos. Chem. Phys.* **2021**, *21*, 9289–9308. [CrossRef]
10. Khairoutdinov, M.; Randall, D. High-Resolution Simulation of Shallow-to-Deep Convection Transition over Land. *J. Atmos. Sci.* **2006**, *63*, 3421–3436. [CrossRef]
11. Wolding, B.; Rydbeck, A.; Dias, J.; Ahmed, F.; Gehne, M.; Kiladis, G.; Dellaripa, E.M.R.; Chen, X.C.; McCoy, I.L. Atmosphere–Ocean Coupled Energy Budgets of Tropical Convective Discharge–Recharge Cycles. *J. Atmos. Sci.* **2024**, *81*, 3–29. [CrossRef]
12. Zhuang, Y.; Fu, R.; Wang, H. How Do Environmental Conditions Influence Vertical Buoyancy Structure and Shallow-to-Deep Convection Transition across Different Climate Regimes? *J. Atmos. Sci.* **2018**, *75*, 1909–1932. [CrossRef]
13. Shin, H.H.; Xue, L.L.; Li, W.W.; Firl, G.; D'Amico, D.F.; Muñoz-Esparza, D.; Ek, E.K.; Chu, Y.F.; Wang, Z.E.; Gustafson, W.I.; et al. Large-Scale Forcing Impact on the Development of Shallow Convective Clouds Revealed from LASSO Large-Eddy Simulations. *JGR Atmos.* **2021**, *126*, e2021JD035208. [CrossRef]
14. Xu, G.; Fu, S.; Liu, J.; Shang, R.; Luo, Y. A Satellite Observational Study of Topographical Effects on Daytime Shallow Convective Clouds. *Remote Sens.* **2023**, *15*, 5542. [CrossRef]
15. IPCC. *Climate Change 2021: The Physical Science Basis. Contribution of Working Group I to the Sixth Assessment Report of the Intergovernmental Panel on Climate Change*; Cambridge University Press: Cambridge, UK, 2021.
16. Schemann, V.; Ebell, K.; Pospichal, B.; Neggers, R.; Moseley, C.; Stevens, B. Linking Large-Eddy Simulations to Local Cloud Observations. *J. Adv. Model. Earth Syst.* **2020**, *12*, e2020MS002209. [CrossRef]
17. Janssens, M.; George, G.; Schulz, H.; Couvreux, F.; Bouniol, D. Shallow Convective Heating in Weak Temperature Gradient Balance Explains Mesoscale Vertical Motions in the Trades. *JGR Atmos.* **2024**, *129*, e2024JD041417. [CrossRef]
18. Randall, D.A. Beyond deadlock. *Geophys. Res. Lett.* **2013**, *40*, 5970–5976. [CrossRef]
19. Berg, L.K.; Gustafson, W.I.; Kassianov, E.I.; Deng, L. Evaluation of a Modified Scheme for Shallow Convection: Implementation of CuP and Case Studies. *Mon. Weather Rev.* **2013**, *141*, 134–147. [CrossRef]
20. Neggers, R.A.J. Exploring bin-macrophysics models for moist convective transport and clouds. *J. Adv. Model. Earth Syst.* **2015**, *7*, 2079–2104. [CrossRef]
21. Suselj, K.; Kurowski, M.J.; Teixeira, J. On the Factors Controlling the Development of Shallow Convection in Eddy-Diffusivity /Mass-Flux Models. *J. Atmos. Sci.* **2019**, *76*, 433–456. [CrossRef]

22. Peters, J.M.; Morrison, H.; Zhang, G.J.; Powell, S.W. Improving the Physical Basis for Updraft Dynamics in Deep Convection Parameterizations. *J. Adv. Model. Earth Syst.* **2021**, *13*, e2020MS002282. [CrossRef]
23. Dogra, G.; Bera, S.; Dewan, A.; Sahany, S. Understanding Dynamical Properties of Cumulus Clouds Over the Bay of Bengal. *Pure Appl. Geophys.* **2023**, *180*, 2915–2926. [CrossRef]
24. Dawe, J.T.; Austin, P.H. Statistical Analysis of An LES Shallow Cumulus Cloud Ensemble Using a Cloud Tracking Algorithm. *Atmos. Chem. Phys.* **2012**, *12*, 1101–1119. [CrossRef]
25. Rousseau-Rizzi, R.; Kirshbaum, D.J.; Yau, M.K. Initiation of Deep Convection over an Idealized Mesoscale Convergence Line. *J. Atmos. Sci.* **2017**, *74*, 835–853. [CrossRef]
26. LeMone, M.A.; Pennell, W.T. The Relationship of Trade Wind Cumulus Distribution to Subcloud Layer Fluxes and Structure. *Mon. Weather Rev.* **1976**, *104*, 524–539. [CrossRef]
27. Stull, R.B. *An Introduction to Boundary Layer Meteorology*, 1st ed.; Kluwer Academic Publishers: Dordrecht, The Netherlands, 1988.
28. Griewank, P.J.; Heus, T.; Lareau, N.P.; Neggers, R.A.J. Size Dependence in Chord Characteristics from Simulated and Ob served Continental Shallow Cumulus. *Atmos. Chem. Phys.* **2020**, *20*, 10211–10230. [CrossRef]
29. Griewank, P.J.; Heus, T.; Neggers, R.A.J. Size-Dependent Characteristics of Surface-Rooted Three-Dimensional Convective Objects in Continental Shallow Cumulus Simulations. *J. Adv. Model. Earth Syst.* **2022**, *14*, e2021MS002612. [CrossRef]
30. Lee, J.M.; Zhang, Y.; Klein, S.A. The Effect of Land Surface Heterogeneity and Background Wind on Shallow Cumulus Clouds and the Transition to Deeper Convection. *J. Atmos. Sci.* **2019**, *76*, 401–419. [CrossRef]
31. Avissar, R.; Schmidt, T. An Evaluation of the Scale at which Ground-Surface Heat Flux Patchiness Affects the Convective Boundary Layer Using Large-Eddy Simulations. *J. Atmos. Sci.* **1998**, *55*, 2666–2689. [CrossRef]
32. Rotach, M.W.; Wohlfahrt, G.; Hansel, A.; Reif, M.; Wagner, J.; Gohm, A. The World is Not Flat: Implications for the Global Carbon Balance. *Bull. Am. Meteorol. Soc.* **2014**, *95*, 1021–1028. [CrossRef]
33. Gong, M.; Fu, S.; Liu, J.; Deng, X. A Modeling Study of the Topographic Effects on Shallow Convective Clouds. *Earth Space Sci.* **2025**, *12*, e2024EA003867. [CrossRef]
34. Fu, S.; Rotunno, R.; Xue, H. Response of Orographic Precipitation to Subsaturated Low-Level Layers. *J. Atmos. Sci.* **2019**, *76*, 3753–3771. [CrossRef]
35. Gopalakrishnan, S.G.; Roy, S.B.; Avissar, R. An Evaluation of the Scale at which Topographical Features Affect the Convective Boundary Layer Using Large Eddy Simulations. *J. Atmos. Sci.* **2000**, *57*, 334–351. [CrossRef]
36. Bryan, G.H.; Fritsch, J.M. A Benchmark Simulation for Moist Nonhydrostatic Numerical Models. *Mon. Weather Rev.* **2002**, *130*, 2917–2928. [CrossRef]
37. Skamarock, W.C.; Klemp, J.B. Efficiency and Accuracy of the Klemp-Wilhelmson Time-Splitting Technique. *Mon. Weather Rev.* **1994**, *122*, 2623–2630. [CrossRef]
38. Wicker, L.J.; Skamarock, W.C. Time-Splitting Methods for Elastic Models Using Forward Time Schemes. *Mon. Weather Rev.* **2002**, *130*, 2088–2097. [CrossRef]
39. Borges, R.; Carmona, M.; Costa, B.; Don, W.S. An improved weighted essentially non-oscillatory scheme for hyperbolic conservation laws. *J. Comput. Phys.* **2008**, *227*, 3191–3211. [CrossRef]
40. Gal-Chen, T.; Somerville, R.C. On the Use of a Coordinate Transformation for the Solution of the Navier-Stokes Equations. *J. Comput. Phys.* **1975**, *17*, 209–228. [CrossRef]
41. Deardorff, J.W. Stratocumulus-capped mixed layers derived from a three-dimensional model. *Bound.-Layer Meteorol.* **1980**, *18*, 495–527. [CrossRef]
42. Morrison, H.; Curry, J.A.; Khvorostyanov, V.I. A New Double-Moment Microphysics Parameterization for Application in Cloud and Climate Models. Part I: Description. *J. Atmos. Sci.* **2005**, *62*, 1665–1677. [CrossRef]
43. Zhu, Z.; Woodcock, C.E. Object-Based Cloud and Cloud Shadow Detection in Landsat Imagery. *Remote Sens. Environ.* **2012**, *118*, 83–94. [CrossRef]
44. Hersbach, H.; Bell, B.; Berrisford, P.; Hirahara, S.; Horányi, A.; Muñoz-Sabater, J.; Nicolas, J.; Peubey, C.; Radu, R.; Schepers, D.; et al. The ERA5 global reanalysis. *Q. J. R. Meteorol. Soc.* **2020**, *146*, 1999–2049. [CrossRef]
45. Kirshbaum, D.J. Cloud-Resolving Simulations of Deep Convection over a Heated Mountain. *J. Atmos. Sci.* **2011**, *68*, 361–378. [CrossRef]
46. Rampanelli, G.; Zardi, D.; Rotunno, R. Mechanisms of Up-Valley Winds. *J. Atmos. Sci.* **2004**, *61*, 3097–3111. [CrossRef]
47. Jiang, H.; Xue, H.; Teller, A.; Feingold, G.; Levin, Z. Aerosol Effects on the Lifetime of Shallow Cumulus. *Geophys. Res. Let.* **2006**, *33*, 2006GL026024. [CrossRef]
48. Xue, H.; Feingold, G.; Stevens, B. Aerosol Effects on Clouds, Precipitation, and the Organization of Shallow Cumulus Convection. *J. Atmos. Sci.* **2008**, *65*, 392–406. [CrossRef]
49. Jacob, M.; Kollias, P.; Ament, F.; Schemann, V.; Crewell, S. Multilayer Cloud Conditions in Trade Wind Shallow Cumulus –Confronting two ICON Model Derivatives with Airborne Observations. *Geosci. Model. Dev.* **2020**, *13*, 5757–5777. [CrossRef]
50. Fu, S.; Rotunno, R.; Xue, H. Convective Updrafts Near Sea-Breeze Fronts. *Atmos. Chem. Phys.* **2022**, *22*, 7727–7738. [CrossRef]

51. Zhang, G.J.; McFarlane, N.A. Sensitivity of Climate Simulations to the Parameterization of Cumulus Convection in the Canadian Climate Centre General Circulation Model. *Atmos. Ocean* **1995**, *33*, 407–446. [CrossRef]
52. Whiteman, C.D. *Mountain Meteorology: Fundamentals and Applications*; Oxford University Press: Oxford, UK, 2000.
53. Bryan, G.H. *Cloud Model 1, Release 19.10*; National Center for Atmospheric Research (NCAR): Boulder, CO, USA, 2020. Available online: https://www2.mmm.ucar.edu/people/bryan/cm1 (accessed on 10 December 2023).
54. University of Wyoming Atmospheric Science Radiosonde Archive. 2023. Available online: https://weather.uwyo.edu/upperair/sounding.shtml (accessed on 15 December 2023).
55. Copernicus Climate Change Service. ECMWF Reanalysis v5 (ERA5). 2023. Available online: https://www.ecmwf.int/en/forecasts/dataset/ecmwf-reanalysis-v5 (accessed on 20 December 2023).

Disclaimer/Publisher's Note: The statements, opinions and data contained in all publications are solely those of the individual author(s) and contributor(s) and not of MDPI and/or the editor(s). MDPI and/or the editor(s) disclaim responsibility for any injury to people or property resulting from any ideas, methods, instructions or products referred to in the content.